広島大学 学位論文

# Investigation of Local Ferroelectric Order in Strontium Titanate by using X-ray Spectroscopy

X 線分光法による $SrTiO_3$ の局所的強誘電性秩序の研究

2017 年

広島大学大学院理学研究科
物理科学専攻

Cong Lu

# 目次

- **主論文**

**Investigation of Local Ferroelectric Order in Strontium Titanate by using X-ray Spectroscopy**

X 線分光法による $SrTiO_3$ の局所的強誘電性秩序の研究

- **公表論文**

**(1) Observation of the flexoelectricity of a $SrTiO_3$ single crystal by X-ray absorption and emission spectroscopies**

**Cong Lu**, Nobuo Nakajima, and Hiroshi Maruyama

Journal of Physics: Condensed Matter **29** (2017) 045702.

**(2) Isotropic Shrinkage of the Oxygen Octahedron in $SrTiO_3$ under Uniaxial Pressure**

**Cong Lu**, Chisato Temba, Nobuo Nakajima, Shuhei Kawakami, Naoki Ishimatsu, and Hiroshi Maruyama

Journal of Physics: Condensed Matter, Accepted on 10 July 2017.

- **参考論文**

## (1) Dielectric characteristics of cation deficient $TbMnO_3$

**Cong Lu**, Yimin Cui

Physica B: Condensed Matter **407** (2012) 3856.

## (2) Dielectric characteristics of Si-added and Si-doped $TbMnO_3$

**Cong Lu**, Yimin Cui

Physica B: Condensed Matter **432** (2014) 58.

# 主論文

Doctoral Thesis

# Investigation of Local Ferroelectric Order in Strontium Titanate by using X-ray Spectroscopy

Cong Lu

Graduate School of Science

Hiroshima University

2017

## • Abstract

Strontium titanate ($SrTiO_3$) is a typical paraelectric material with a cubic perovskite structure. Ferroelectric order in $SrTiO_3$ induced by structural transformations or external stimuli such as pressure or bending stress has attracted much attention because this material is expected to be useful in lead-free ferroelectric applications. This thesis is the first in a series of investigations to explore the possibility that a local ferroelectric order may be caused by external pressure or structural deformations in single crystals and thin films of pure $SrTiO_3$.

We measured the X-ray absorption spectra at the Ti *K*-edge of a $SrTiO_3$ single crystal under uniaxial pressure were measured to investigate the uniaxial pressure-induced polarization predicted for $SrTiO_3$ from an electronic viewpoint. We found that the pre-edge $3d$ $e_g$ peak decreases in intensity with increasing uniaxial pressure and shifts to the high energy. These changes were independent of the incident X-ray polarization, thus implying the presence of a mechanism to maintain the isotropic coordination environment around a Ti atom, e.g., a tilt and rotation of the $TiO_6$ octahedron that accompanies its isotropic shrinkage. Hence, the local polarization essential to the creation of a ferroelectric order is not observed.

By using X-ray spectroscopy, we also performed a microscopic investigation of flexoelectricity, which is defined as the spontaneous electronic polarization in a dielectric material induced by a strain gradient. We used a single-crystal sample of $SrTiO_3$ as a test system to explore the appearance of an electric dipole moment caused by simple bending of the crystal. We did not observe the spectral changes in the Ti *K*-edge absorption spectra that are characteristic of a ferroelectric transition in $SrTiO_3$. Instead, we observed a gradual decrease (increase) of the second peak (pre-edge structure) caused by bending. This can be qualitatively explained by theoretical

calculations that assume the presence of oxygen vacancies and a slight distortion of the crystal. This assumption is also supported by the broadening of a tiny charge-transfer peak in the Ti *K*β resonant emission spectra. Therefore, we found that the flexoelectric effect in $SrTiO_3$ is easily drowned out by local imperfections induced by crystal deformations and defects.

By using thin films of $SrTiO_3$ prepared by sputtering onto various substrates, we investigated local distortions of the films by using Ti *K*-edge X-ray absorption spectroscopy. In all the films that we studied, enhancements of the Ti 3*d* $e_g$ pre-edge peak due to the off-center displacements of the Ti ions, which indicate the potential for ferroelectricity, were observed. We also observed two minor changes in the spectra depending on the specific films being studied: (1) an enhancement of the main absorption edge and (2) a clear separation of the $e_g$ and $t_{2g}$ peaks. A simple model that simulates these features involves the coexistence of antiferrodistortive rotations of the $TiO_6$ octahedra with local ferroelectric order caused by the off-centering of the Ti atoms.

Through our experimental data and analysis, for the pure quantum paraelectric $SrTiO_3$, the local ferroelectric order with the microscopic view was clarified from XAFS and RXES spectra. The $SrTiO_3$ single crystals both under uniaxial and bending pressure are shown to be substantially free of FE transformation in local region. On the contrary, the sputtered $SrTiO_3$ thin film is confirmed the character of local FE transition as the Ti off-center displacement is investigated as well as the AFD distortion.

# Contents

# 1. Introduction

## 1.1. Physical Properties of STO

### 1.1.1. Basic Characteristics

Perovskite-type oxides are some of the most fascinating materials in condensed-matter research, exhibiting such diverse properties as ferroelectricity, ionic conductivity, catalytic activity, and colossal magnetoresistance [1-4]. The perovskite-type oxide $SrTiO_3$ (STO) is a prototypical member of this structural family. It is a typical perovskite paraelectric material having a high degree of cubic symmetry under ambient conditions (Figure 1-1). The crystal structure is cubic at room temperature, with space group $Pm3m$, and the lattice constant is 3.905 Å [5, 6]. The direct band-gap energy between the Ti 3*d* conduction band and the O 2*p* valence band is 3.4 eV, and the indirect band gap is 3.2 eV. As a typical band insulator, the oxide semiconductor STO and its heterostructures have attracted much attention for energy-harvesting applications. For example, the efficiency of thermoelectric devices can be improved by tuning the band gap or electron mobility [7-10].

STO is also an important technological material due to its high chemical and thermal stability, high dielectric constant, and resistance to oxidation [11]. Generally, the dielectric properties of STO qualitatively resemble those of the paraelectric phase of typical perovskite ferroelectrics such as $BaTiO_3$. In these materials, a soft transverse optical mode exists, the frequency of which tends to zero with decreasing temperature. This leads to an increase in the permittivity of STO when the material is cooled. However, in contrast to $BaTiO_3$, STO is an incipient ferroelectric or a quantum paraelectric, which means that it does not undergo a ferroelectric transition [12, 13].

This is attributed to quantum fluctuations in the material at low temperatures, which suppress the ferroelectric transition. In addition, STO is a fluorescent material that emits visible light under ultraviolet (UV) irradiation [14, 15]. For example, stoichiometric oxygen-deficient STO emits blue light at room temperature.

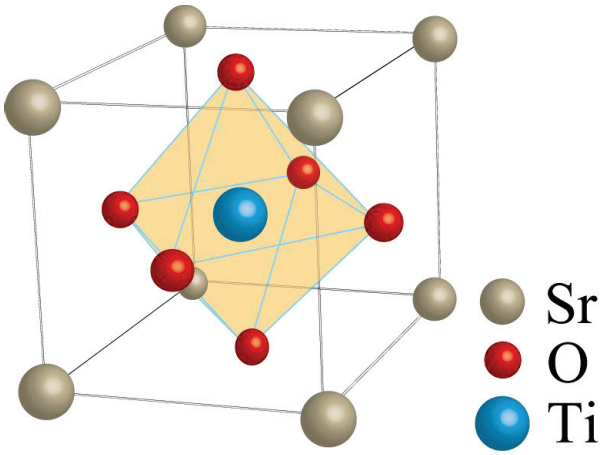


**Figure 1-1**. Crystal structure of STO showing perfect cubic symmetry at room temperature.

### 1.1.2. Splitting of the 3*d* Orbitals and *p*–*d* Hybridization

Crystal-field theory can describe the bonding in metal complexes. In the case of STO, the degeneracy of the five *d*-orbitals is lifted by the octahedral field of the $TiO_6$ complex. The 3*d* orbitals of the Ti ion under $O_h$ symmetry are split into triply-degenerate $t_{2g}$ components and doubly-degenerate $e_g$ components by crystal-field splitting (Figure 1-2). The energy gap between the $t_{2g}$ and $e_g$ states is denoted by $\Delta = 10Dq$ and is called the "crystal-field splitting energy." The $e_g$ orbitals ($x^2–y^2$, $3z^2–r^2$) lie on the same axes as the negative charges and are affected most by the electrostatic interactions. In contrast, the

$t_{2g}$ orbitals (*xy*, *yz*, and *zx*) bisect the negative charges and are less affected (or stabilized) by the electrostatic interactions (Figure 1-3) [16].

The term "*p–d* hybridization" refers to a merging of the separate *p* and *d* atomic orbitals to form the same total number of hybrid orbitals [17, 18]. Previous research has demonstrated that ferroelectricity in $BaTiO_3$ is sensitive to hybridization between the O 2*p* orbital and the empty 3*d* orbital of the Ti ions [19]. Therefore, it is reasonable to assume that hybridization of the 3*d* orbitals of Ti with the 2*p* orbitals of O in STO may occur in a ferroelectric transition.

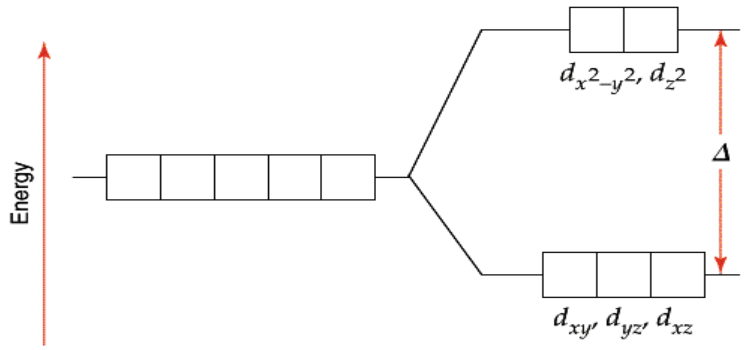


**Figure 1-2**. Crystal-field splitting of 3*d* electronic orbitals under $O_h$ symmetry.

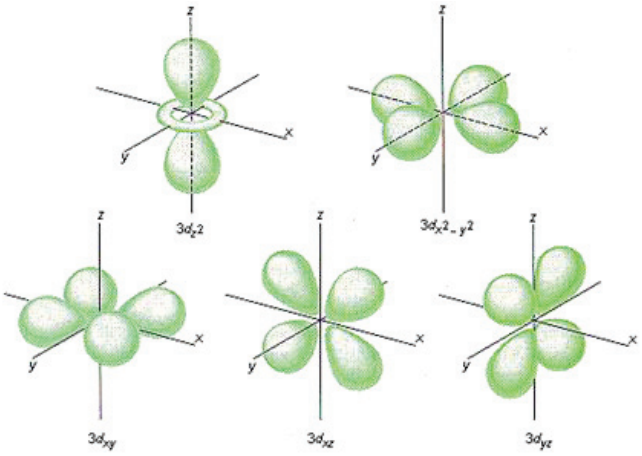


**Figure 1-3**. 3*d* electron cloud distributions of the $t_{2g}$ (*xy*, *yz*, *zx*) and $e_g$ ($3z^2–r^2$, $x^2–y^2$) orbitals.

### 1.1.3. Ferroelectric and Antiferrodistortive Phase Transitions

STO is known to be an incipient paraelectric material. This means that it exhibits a ferroelectric (FE) instability that, due to quantum fluctuations, is too weak to manifest itself even at the lowest attainable temperatures. As a result, one of the most important phase transitions to be investigated in STO is the ferroelectric phase transition resulting from the polar displacement of $Ti^{4+}$ and $O^{2-}$ against one another. STO shows many signs that it is approaching a ferroelectric state as the temperature is lowered toward 0 K. Pressure has been shown to stabilize a ferroelectric phase in STO above 0 K [20], as have chemical and even isotopic substitutions [21-23]. The most spectacular example is room-temperature ferroelectricity in STO films strained by a large biaxial tension [24].

In the temperature range below 105 K, STO enters into an antiferrodistortive (AFD) regime. This is a very important type of phase transition in STO, which involves small rotations of the $TiO_6$ octahedra. In this case, the $TiO_6$ octahedra rotate about one of the axes to cause a transformation from a cubic structure to a tetragonal structure. Alternate

layers of octahedra normal to the *c*-axis rotate in opposite directions. The structures associated with the AFD transition in STO are illustrated in Figure 1-4 [25].

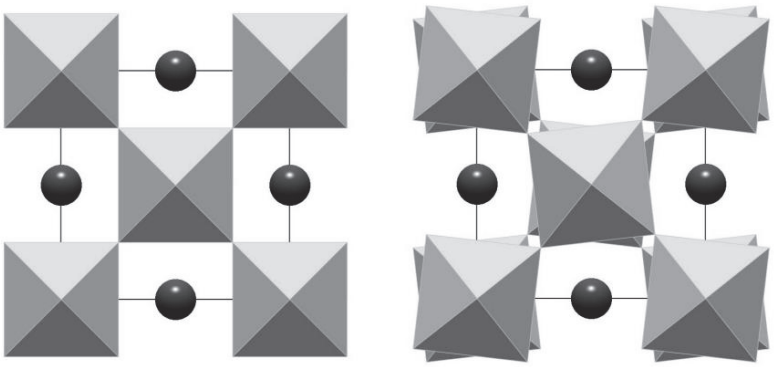

**Figure 1-4.** The left-hand figure shows the structure of the standard cubic phase of STO, while the right-hand figure shows the rotations of the $TiO_6$ octahedra (the AFD transition) associated with the FE phase transition in STO [25].

## 1.2. Electric Dipole Moments induced in STO

STO is well known to be a nearly ferroelectric material in what is called a "quantum paraelectric" state. This means that dielectric polarization may arise owing to a number of conditions. The quantum paraelectric state is very sensitive to perturbations of the lattice. For this reason, a ferroelectric transition can be induced in STO in many ways such as adding small levels of impurities (doping), applying electric fields, irradiating with UV light, isotope substitution, subjecting to mechanical stress, and so on [26-28].

### 1.2.1. Flexoelectricity

In recent years, there has been increasing interest in investigating the electromechanical coupling termed "flexoelectricity" (FxE) [29, 30]. This effect is defined as the presence of spontaneous polarization induced by a strain gradient. Unlike ferroelectricity, which is present only in non-centrosymmetric materials, FxE can exist in both non-centrosymmetric and centrosymmetric materials. This broadens the range of possible flexoelectric materials. While FxE was originally proposed approximately 50 years ago because the effect is relatively weak, only a few studies focusing on it have been performed during the previous century. Subsequently, based on macroscopic measurements, Ma and Cross reported that the value of the flexoelectric coefficient can be on the order of μC $m^{-1}$ [31]. In addition to experimental investigations, theoretical studies have led to an increased understanding of FxE, first from a phenomenological perspective and later by using first-principles calculations [32, 33]. The comparison between FxE and piezoeelecticity on definition and physical description is listed in the following Table 1-1:

**Table 1-1**. The comparison between FxE and piezoeelecticity.

| Piezoelectricity (圧電性) | Flexoelectricity (撓電性) |
|---|---|
| $P_i = \boldsymbol{dijk}\,\sigma_{jk}$ | $P_l = \mu_{ijkl}\,\partial\varepsilon_{ij}/\partial x_k$ |
| Only allowed for noncentrosymmetric systems of 20 point groups | Can exist in all 32 point groups |
| Under $T_c$ | No limitation |
| Wisely Application in energy converter and transducer | Only preliminary theory and experimental research |
| strain | Strain gradient |

Zubko *et al*. have measured the dielectric polarization induced by bending in single crystals of STO [34]. All the components of the flexoelectric tensor can be determined from measurements of FxE. Figure 1-5 shows an experimental setup for flexoelectric measurements. A dynamical mechanical analyzer with an insulating quartz probe is used to induce oscillatory bending in a sample and measure its amplitude. As shown in Figure 1-6, the polarization induced by a static force, which distorts the local symmetry around a Ti atom, leads to the formation of dipole moments. All the components of the flexoelectric tensor were determined, and calculations based on these results indicate the existence of FxE.

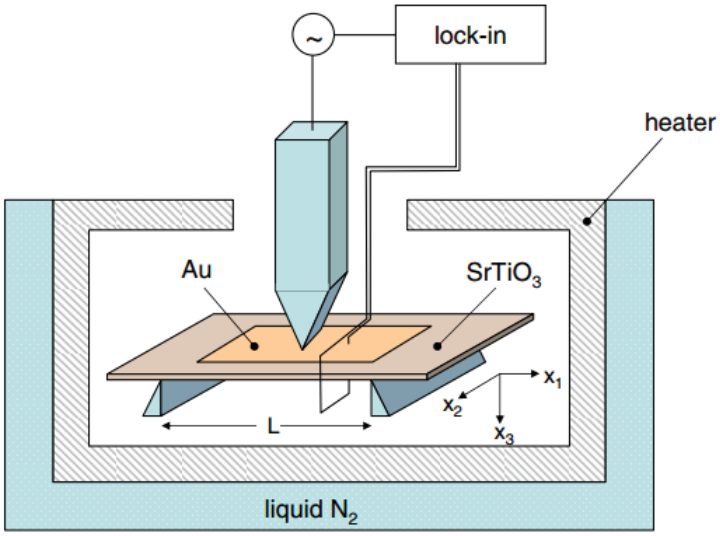


**Figure 1-5.** Experimental setup for flexoelectric measurements on a single crystal of STO [34].

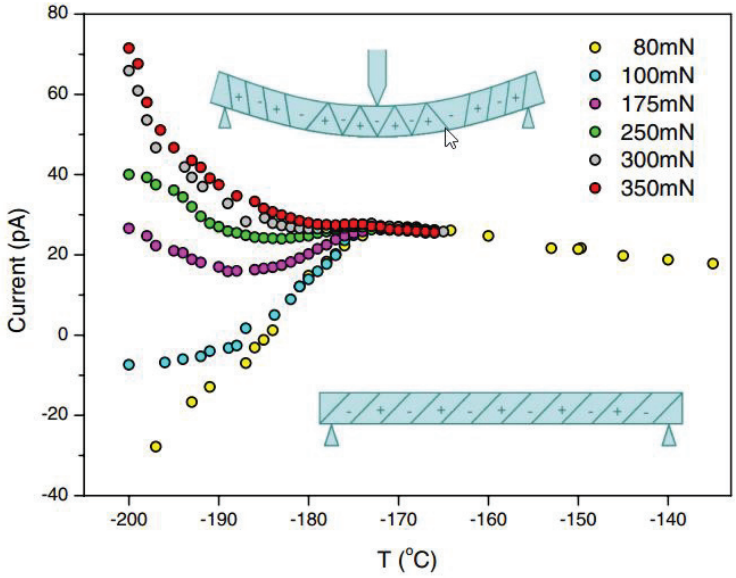


**Figure 1-6.** Temperature- and static-force-dependence of the flexoelectric current of a single crystal of STO [34].

## 1.2.2. Ferroelectric Transition under Uniaxial Force

Figure 1-7 shows the ferroelectric/paraelectric phase diagram under uniaxial force. The temperature-stress curve was obtained by observing optical second-harmonic generation (SHG) [35], which is a sensitive indicator of centricity in crystals. This method enables a more accurate determination of the Curie temperature $T_c$ than that obtained by observing the peak of the dielectric constant $\varepsilon$. Schneider *et al* [36]. have studied quantum-theoretically the properties of the phase transitions at $T_c \approx 0$ caused by variations of parameters in a lattice-dynamical system. They showed that $T_c$ can be expressed in terms of an interaction parameter $S$, which is a function of model parameters:

$$T_c=(S-S_c)^{\frac{1}{2}} \quad , \tag{1-1}$$

where $S_c$ denotes the value of $S$ corresponding to $T_c$ = 0 K. Equation (1-1) applies in the quantum regime, which coincides with that of the experimental investigations using SHG.

From the fluorescence spectra of $Cr^{3+}$-doped STO, Tsujimi *et al.* [37] found that when uniaxial pressure was applied along the $[010]_c$ direction, the tetragonal *c*-axis became perpendicular to the $[010]_c$ direction in both the quantum paraelectric state and the quantum ferroelectric state (QFS). This means that two domains must appear in the quantum paraelectric state. Figure 1-8 shows the increase in the peak intensity of the transverse acoustic mode, which indicates that the spontaneous polarization is not parallel to the cubic *a, b, c* axes in the QFS [37].

Tsujimi *et al*. also found that the broad doublet loses its intensity upon approaching the QFS; the longitudinal acoustic mode softens slightly. These results imply that the pressure-induced QFS of STO may be similar to the temperature-induced QFS of $SrTi^{18}O_3$.

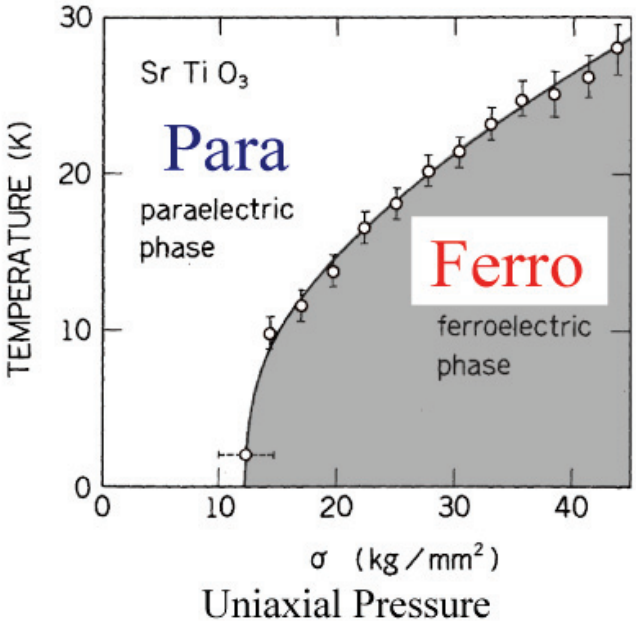


**Figure 1-7.** Temperature-uniaxial stress phase diagram for STO [35].

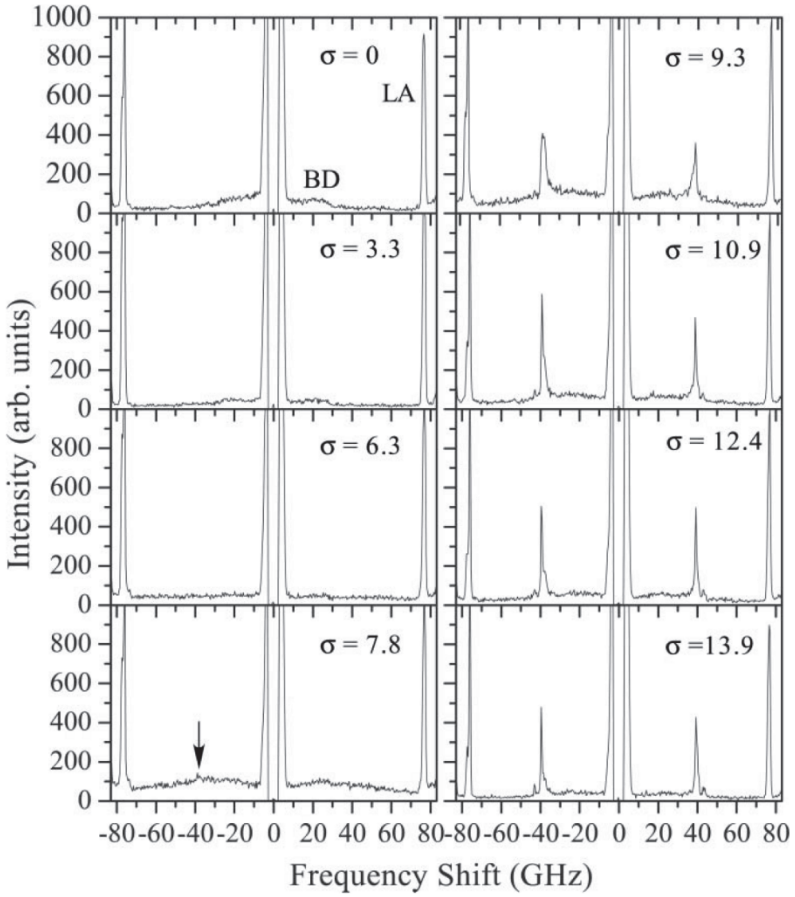


**Figure 1-8.** Typical uniaxial pressure dependence of the Brillouin scattering spectra [37].

## 1.2.3. Ferroelectric Transition in STO Thin Films

In addition to bulk samples, thin films of STO are considered to be good candidates to undergo conversion into a ferroelectric phase over quite a wide temperature range through symmetry breaking.

Quasi-amorphous phases of STO, deposited by radio frequency sputtering, have been shown to stabilize into noncrystalline polar phases that completely deviate from cubic symmetry (Figures 1-9 and 1-10). The formation and microscopic origins of the polarity

can be described by the theory of random networks of local bonding units theory describing the formation and microscopic origin of polarity (Figure 1-8 and 1-9). The discovery of quasi-amorphous materials has opened up a new direction for materials design, since the search for novel pyro- and piezoelectric solids is no longer limited to crystalline compounds with non-centrosymmetric symmetry [38, 39].

Strain, caused by the lattice mismatch between film and substrate, is inevitably generated during the formation of a film and is considered to be the main reason why the properties of thin films differ from those of bulk samples. As shown in Figure 1-11, an STO thin film grown by a heteroepitaxial process has a substantial influence on the establishment of FE order in a phase transition [40]. The lattice-mismatch strain can be divided into "compressive" and "tensile" categories, which dictate the distinct symmetry decrease and polarity order, respectively.

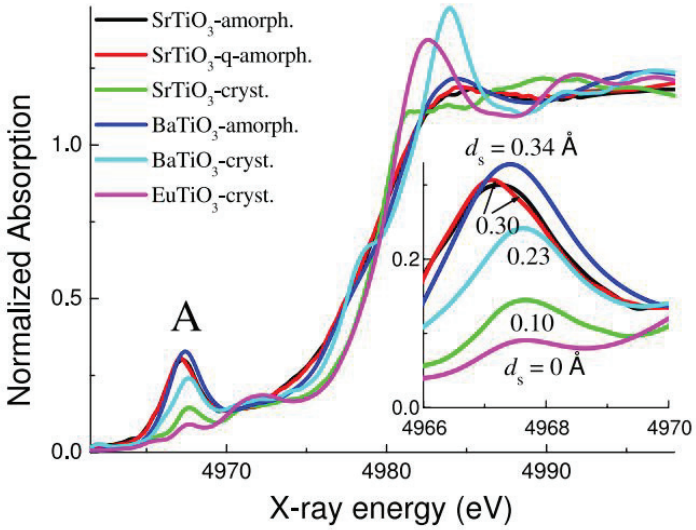


**Figure 1-9.** Comparison of Ti *K*-edge XANES spectra of crystalline, amorphous, and quasi-amorphous STO [38].

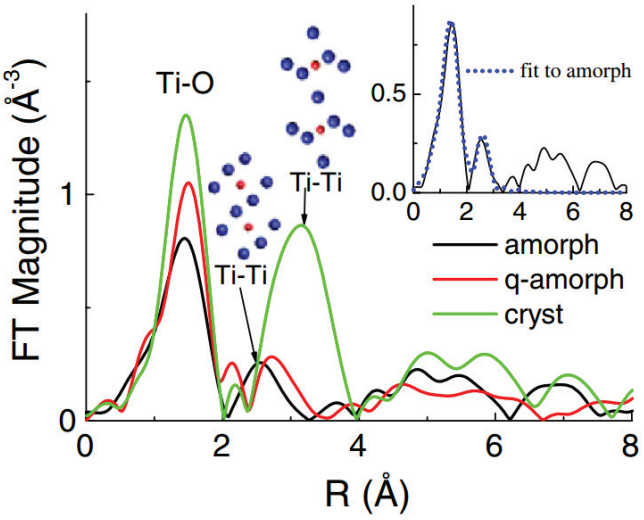


**Figure 1-10.** Magnitudes of the Fourier transforms of the $k^2$-weighted EXAFS spectra of crystalline, amorphous, and quasi-amorphous STO [38].

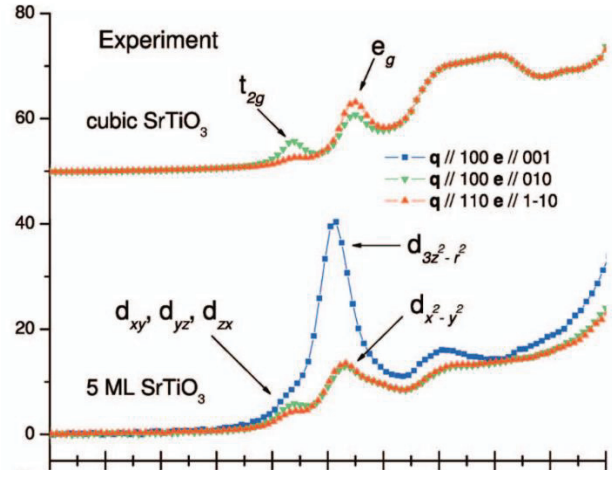


**Figure 1-11.** Comparison of Ti *K*-edge spectra for cubic STO and for a five-monolayer (ML) STO thin film [40].

## 1.3. The Outline of This Thesis

### 1.3.1. Research Background

Ferroelectric materials exhibit strong polarization under external stimuli and structural deformations, which are accompanied by technologically advantageous phenomena such as piezoelectricity, electrostriction, and flexoelectricity. Together with global symmetry breaking, these are the macroscopic effects that result from local ordering. Researchers have used various approaches to study the possibilities of ferroelectric-transition phenomena in STO, especially effects caused by external pressure or by introducing strain into thin films. For a long time, the research community focused on a macroscopic approach to the dielectric properties of this material. However, we expect that the investigation of local symmetry effects can lead to new physical insights into the ferroelectric phase transition and the role of microscopic distortions. The perovskite form of STO exhibits properties of high-temperature dielectrics that are considered to be promising candidates for lead-free ferroelectric applications. In this thesis, I explore symmetry-breaking in cubic perovskite STO caused by external pressure and structural deformations in order to understand better the mechanism of local structural distortion and to help accelerate progress towards applications in portable electronic devices.

### 1.3.2. Research Purposes

Two research questions are addressed in this work: First, is local ferroelectric order induced in a single crystal of STO under uniaxial pressure and bending deformation?

Second, how does the local structural picture change in a sputtered STO thin film using different substrates (MgO, $LaAlO_3$, $SiO_2$, and glass)? The purposes of the research are:

(1) For STO samples under different external and internal conditions, to investigate the local electronic state around the Ti atoms using XAFS and RXES measurements.

(2) To use the dependence of the $e_g$ peaks in XAFS and of charge-transfer excitation in RXES to indicate the displacement of the Ti ion from the center of the surrounding O ions in STO.

(3) Finally, to employ analyses and calculations to reveal the mechanisms responsible for local ferroelectric order and lattice distortion.

The purpose of this research is to explore solutions to make the pure STO from paraelectricity to the ferroelectricity at room temperature. This research plays an important role in both basis and application and illustrates the problem of basic physical properties, which points out the direction for exploration of next generation lead-free ferroelectric materials.

# 2. Experimental Techniques

## 2.1. X-ray Spectroscopy

### 2.1.1. X-ray Absorption Fine Structure Spectroscopy

X-ray absorption fine structure spectroscopy (XAFS) refers to the details of X-ray absorption by an atom at energies near and above its core-level binding energies; it is the oscillatory structure in the X-ray absorption coefficient just above an X-ray absorption edge. This turns out to be a unique signature of a given material, and it depends on the detailed atomic structure and electronic and vibrational properties of the material. For this reason, XAFS is a very important probe of materials, revealing information about local atomic structure [41-43].

The left-hand panel of Figure 2-1 is a schematic diagram of an X-ray absorption spectrum (XAS). The several jumps in the absorption coefficient correspond to various absorption edges. In the right-hand panel of Figure 2-1, the *K*-edge XAS spectrum is divided into two regions: the X-ray absorption near-edge structure (XANES) and the region of extended X-ray absorption fine structure (EXAFS).

Formally, the theory of XAS is based on Fermi's golden rule:

$$\mu \propto \sum \left|\langle \psi_f | H' | \psi_j \rangle\right|^2 \delta\left(E_f - E_i - h\omega\right). \qquad (2\text{-}1)$$

The μ is transition probability of an electron. An atom is initially in its ground state $|\psi_i\rangle$ with energy $E_i$. When interacting with the electromagnetic field, the atom can absorb an X-ray photon of energy $\hbar\omega$ and undergo a transition to a final state $|\psi_f\rangle$ with energy $E_f = E_i + \hbar\omega$. The photon energy promotes an electron from a core level to an unoccupied level (excitation) or to the continuum of free states (ionization). The

atomic final state is characterized by the presence of a core hole.

XANES spectroscopy using synchrotron radiation is a well-established technique for providing information about the electronic, structural, and magnetic properties of matter. In XANES, a photon is absorbed and an electron is excited from a core state to an empty state. To excite an electron from a given core level, the photon energy must be equal to or higher than the binding energy of this core level. Thus, a new absorption channel opens each time the photon energy exceeds the binding energy of a level. The energy of an absorption edge therefore corresponds to the core-level energy, which is characteristic for each element, making XANES an element-selective technique.

Conversely, EXAFS stands for "extended X-ray absorption fine structure" that is the region of the spectrum corresponding to energies above the XANES region (see Figure 2-1[b]). The physical origin of EXAFS is electron scattering, which starts immediately past an absorption edge and extends up to about 1 keV above the edge. EXAFS is best thought of as a spectroscopically-detected scattering method, rather than as a more conventional spectroscopy.

XAFS spectra can be measured in both transmission and fluorescence modes, which are illustrated in Figure 2-2. The transmission mode is the most straightforward; it simply involves measuring the X-ray flux both before and after the beam passes through a uniform sample. Absorption coefficient μ is directly observed using transmission measurements. The transmitted flux $I$ is related to the incident flux $I_0$ by the expression:

$$\mu = \ln\left(\frac{I_0}{I_1}\right). \tag{2-2}$$

In the fluorescence mode, one measures the incident flux $I_0$ and the fluorescence X-rays $I_1$ that are emitted following the X-ray absorption event (Figure 2-3). Usually, the fluorescence detector is placed in the horizontal plane at 90° to the incident beam, with the sample at an angle (usually 45°) with respect to the beam. The fluorescence yields of X-rays and of Auger electrons are proportional to the X-ray absorption

coefficient. For this reason, the XAS fluorescence spectrum is expressed as:

$$\mu \propto \frac{I_1}{I_0}. \tag{2-3}$$

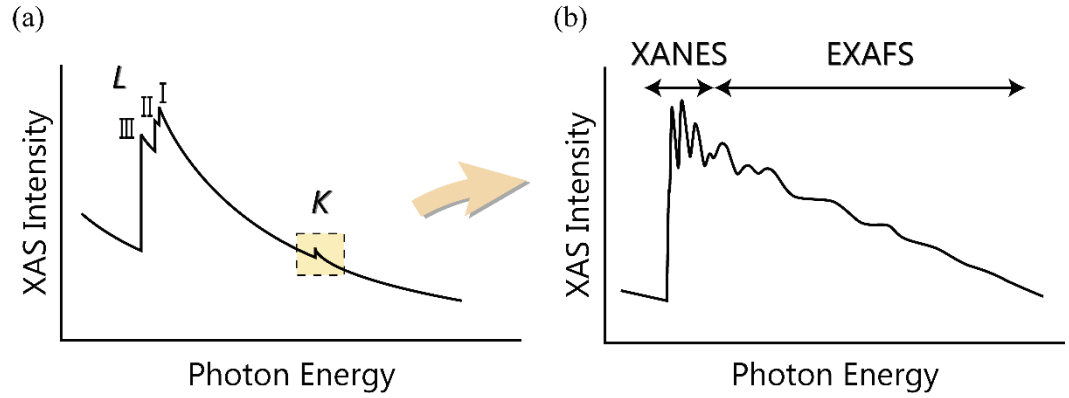


**Figure 2-1.** The left-hand panel is a schematic diagram of the dependence of X-ray absorption on incident photon energy. The right-hand panel shows a typical Ti *K*-edge XAS spectrum.

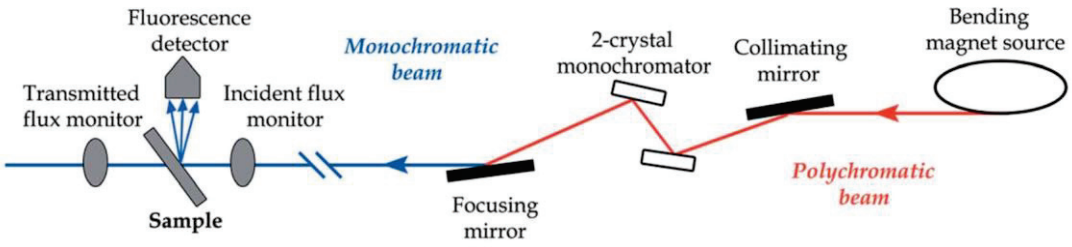


**Figure 2-2.** Layout of the general setup for an XAS experiment.

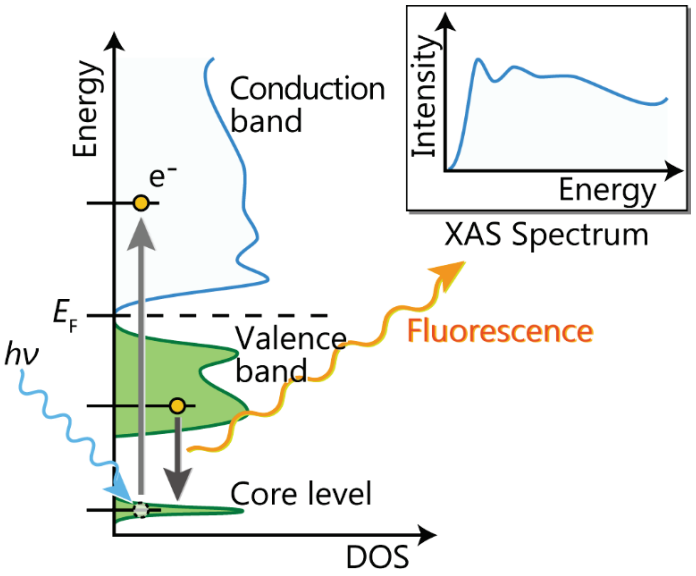


**Figure 2-3.** Schematic diagram of XAS measurement in the fluorescence mode.

### 2.1.2. Resonant X-ray Emission Spectroscopy

The final state in XAS is an excited state with a lifetime $\tau_n$. As soon as a core hole is established by an incident X-ray photon, an outer-shell electron will drop down to occupy it by emitting either a photon (radiative decay) or an electron (non-radiative decay). Recording the emitted X-rays by means of an instrument with an energy bandwidth on the order of the core-hole lifetime is called "X-ray emission spectroscopy" (XES). The decay of an XAS excited state back to the ground state is in most cases a cascade decay with several intermediate states. Because it is a photon-in/photon-out spectroscopy, XES may provide considerably more detailed information about the electronic structure than standard XAS, and the measurements can be performed even with the sample being under an external magnetic or electric field.

If a core electron is resonantly excited to the absorption threshold by the incident photon (as in the process of X-ray absorption spectroscopy), the resulting emission

spectrum depends strongly on the energy of the incident-photon. We designate this type of XES as "resonant X-ray emission spectroscopy" (RXES). Here, we consider just the first decay and describe XES as a second-order optical process that includes RXES. This technique has recently come to the fore as a fine probe of the bulk electronic structures of solid; it relies on the resonant enhancement of excitations to specific intermediate states by a proper choice of the incident photon energy [44, 45]. Figure 2-4 shows a schematic picture of a transition-metal *K*-edge RXES process. The absorption of an incident photon causes the dipole transition of an electron from the 1*s* orbital to the 4*p* orbital, leaving behind a 1*s* core hole (pathway [a] in the figure). In an intermediate state, a 3*d* electron interacts with the 1*s* core hole and the photoexcited 4*p* electron *via* Coulomb interactions, so that excitations in the 3*d* electron system are involved (pathway [b] in the figure). The 4*p* electron returns to the 1*s* orbital again (pathway [c] in the figure), and a photon is emitted, with the differences in energy and momentum between the incident and emitted photons transferred to the 3*d* electron system.

Because the energy $\hbar\omega$ lost by the photon and transferred to the material is independent of the incoming photon energy $\hbar\omega_k$, the set of RXES features appear as vertical lines in a plot of the transferred energy $\hbar\omega$ versus the incoming energy $\hbar\omega_k$. This implies that when the incident photon energy is increased, the energy of the outgoing photons increases by the same amount. This is similar to Stokes phonon losses measured in optical Raman scattering. Using this analogy, one can refer to these energy-loss peaks as "resonant X-ray Raman features," as shown in Figure 2-5. The Raman peaks in RXES spectra are mainly influenced by orbital hybridization among the constituent elements and reflect low-energy excitations in materials. (Excitations induced by the crystal fields and by charge transfer are described in the following subsection.)

Charge transport in a condensed-matter system is determined by the energy of electrons moving from one site to another. The energy is associated with an electron

hopping from a ligand site to a metal site. We concentrate here on the Ti in STO, in which the $Ti^{4+}$ ion of $TiO_6$ is surrounded by the six nearest-neighbor $O^{2-}$ ions. The ground state configuration has a $3d^0$ electronic distribution. The introduction of external stimuli or dopants creates a $d^1\underline{L}$ state, where $\underline{L}$ represents a ligand hole, with charge transferred from an oxygen atom, which couples with the $3d^0$ state via hybridization [19, 46, 47]. Figure 2-6 shows that this causes a peak to appear on the lower-energy side of the elastic peak, with an energy separation Δ. This peak is due to charge-transfer scattering and is simply called a "CT peak." In this research, we measured the CT peak, focusing on its dependence on the bending of an STO single crystal.

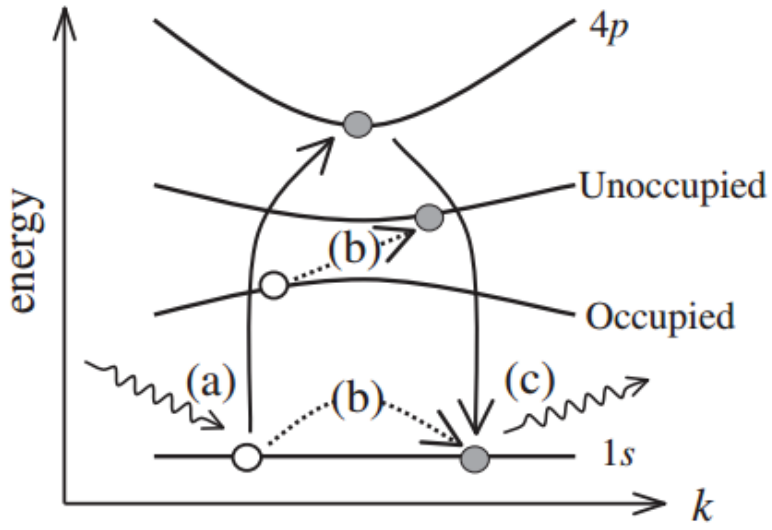


**Figure 2-4.** Schematic picture of a transition metal *K*-edge RXES process.

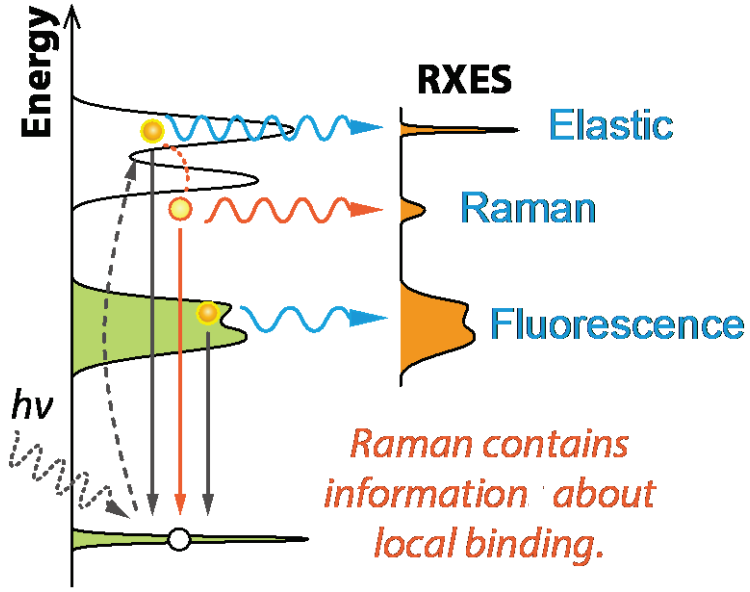


**Figure 2-5.** Schematic diagram of RXES measurements, which shows the Raman structure.

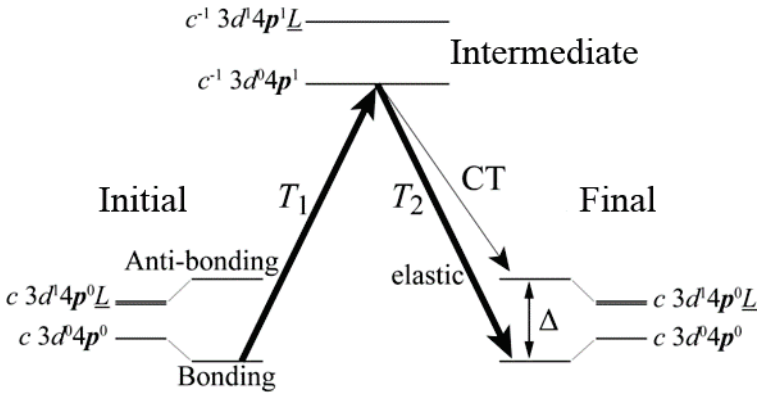


**Figure 2-6.** Schematic RXES energy-level diagram of the charge-transfer process.

## 2.2. Synchrotron Radiation

### 2.2.1. Basic information about Synchrotron Radiation

Relativistic charged particles emit electromagnetic radiation whenever a force is applied to them, causing them to move along curved trajectories. This radiation is called "synchrotron radiation." Today, electron storage rings are routinely employed to provide users with synchrotron radiation over a wide spectral range, from infrared to hard X-rays. Synchrotron radiation has extensive applications in determining material structures and properties in physics, chemistry, and biology, and even in disciplines such as archaeology and environmental science [48, 49]. The main properties of synchrotron radiation are the following:

- High intensity
- Very broad and continuous spectral range from infrared up to the hard X-ray region
- Natural narrow angular collimation
- High degree of polarization
- Pulsed time structure
- High brightness of the source due to the small cross-section of the electron beam and high degree of collimation of the radiation
- Ultra-high vacuum environment and high beam stability
- All properties can be quantitatively evaluated

Three generations of synchrotron-radiation sources, emitting radiation with increasing quality, have been developed to date. With the advent of third-generation synchrotron facilities (see Figure 2-7), which are characterized by the use of insertion devices, particularly undulators, the brilliance available for researchers in the field of X-ray science has jumped by some four orders of magnitude. This enormous increase in

the number of X-ray photons in tightly focused bundles has revolutionized X-ray techniques, enabling the study of increasingly small structures over shorter and shorter timescales.

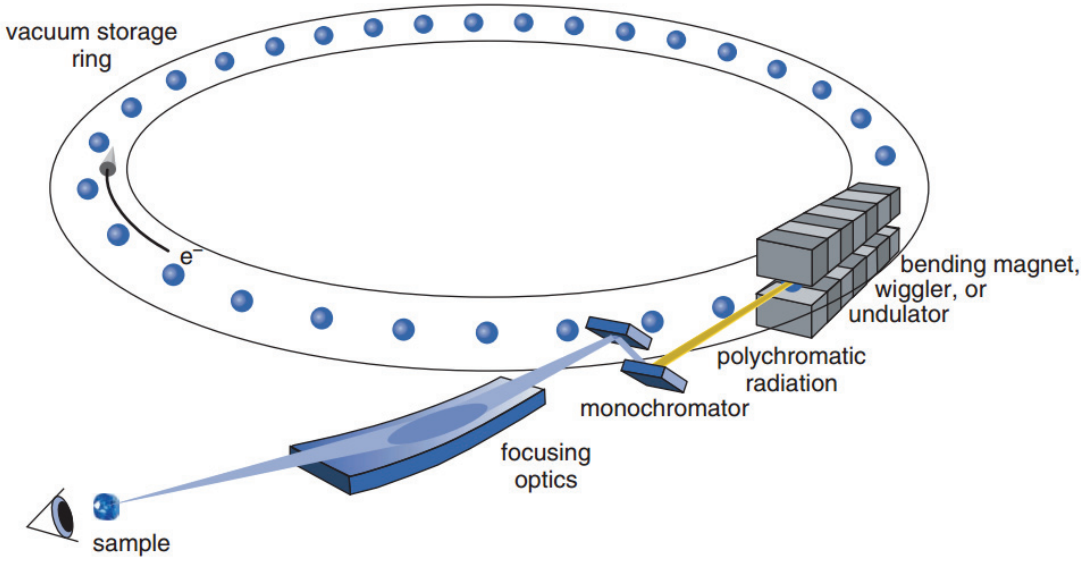


**Figure 2-7.** Schematic of a third-generation synchrotron [48].

## 2.2.2. Undulator Beamline BL39XU at SPring-8

SPring-8 is a large synchrotron-radiation facility, which delivers the most powerful synchrotron radiation currently available. The research conducted at SPring-8 includes nanotechnology, biotechnology, industrial applications, and so on. The name "SPring-8" is derived from "Super Photon ring-8 GeV," with 8 GeV being the power output of the ring. The beam is extracted and run through undulators to produce synchrotron radiation with energies ranging from soft X-rays (300 eV) up to hard X-rays (300 keV) [50].

Our Ti *K*-edge XAS and Ti *Kβ* RXES measurements were performed on the beamline

BL39XU at SPring-8, where various polarization states of X-rays can be used. By adjusting the diamond X-ray phase shifter installed in the beam line, one can easily obtain clockwise and counterclockwise circularly polarized light, horizontal and vertical linearly polarized light, and arbitrary elliptically polarized light. The energy range of X-rays available using a liquid nitrogen cooled Si (111) double-crystal monochromator is 5 to 38 keV (Si 111). A rhodium (Rh) evaporation mirror is used to remove high-order light, reducing its intensity to approximately 40% of the first-order light. A schematic view of BL39XU is shown in Figure 2-8, and the characteristic parameters of the X-rays available for measurements are listed in Table 2-1. Vertically polarized X-rays (parallel to the *ac*-plane), obtained using a 0.1-mm-thick diamond X-ray phase retarder, were irradiated onto the sample. The Ti *K*-edge XAS were obtained in the bulk sensitive fluorescence mode with a silicon drift detector. The Ti *Kβ* RXES spectra were obtained using a spherical curved Ge (331) analyzer crystal and the 2D hybrid pixel array detector PILATUS [51]. The sample holder was placed in a vacuum chamber to prevent X-ray scattering by air. All measurements were performed at room temperature [52].

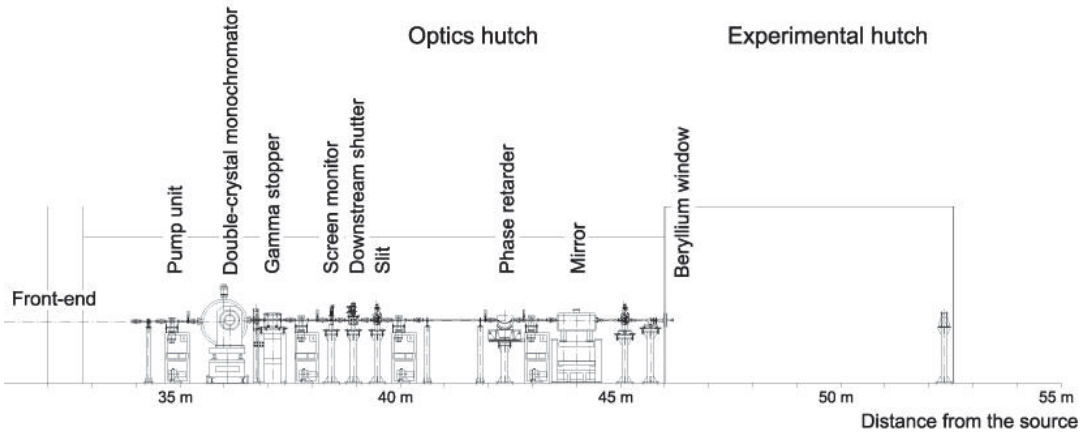


**Figure 2-8.** Beamline layout of BL39XU at SPring-8 [52].

**Table 2-1**. X-rays available at sample in BL39XU at SPring-8 [52].

| | |
|---|---|
| Energy Range | 5~38 keV (Si 111) |
| Energy Resolution ΔE/E | $2 \times 10^{-4}$ (Si 111), $1 \times 10^{-4}$ (Si 220) |
| Photon Number | $5.3 \times 10^{13}$ photons/s (Si 111) |
| Beam Size (FWHM) | 0.6 (V) × 0.6 (H) $mm^2$ |
| High-order light | $<1 \times 10^{-4}$ |
| Linear polarization | 99.9% |
| Circular polarization | >90% |

## 2.2.3. Undulator Beamline BL-9A at the Photon Factory

The High Energy Accelerator Research Organization, KEK, is one of the world's leading accelerator-science research laboratories that uses high-energy particle beams and synchrotron light sources to probe the fundamental properties of matter. The Photon Factory (PF) is a dedicated synchrotron-radiation facility affiliated with the National Laboratory for High Energy Physics, KEK, Tsukuba Academic City, located approximately 60 km north-east of Tokyo. The accelerator complex consists of a 2.5-GeV electron linear accelerator and a 2.5-GeV electron-storage ring, the PF, which usually stores 2.5-GeV electron beams in a multi-bunch operation. Parts of the scheduled operation are also performed in a single-bunch mode or in a relatively high-energy (3 GeV) operation with a top-up mode. Some beamlines have an undulator or a wiggler as insertion devices, which are utilized for experimental purposes [53].

Our Ti *K*-edge XAFS experiments were implemented at the high-intensity, low-energy XAFS beamline BL-9A of the Photon Factory (Figure 2-8) at the Institute of Materials Structure Science (KEK-PF), for which the X-ray energy was regulated using a Si (111) double-crystal monochromator to cover the photon energy range from 2.1 to 15 keV. The X-ray specifications are listed in Table 2-2. In this study, all spectra were

obtained using a horizontal configuration at room temperature. The angular position of the monochromator crystals was calibrated using the Ti *K*-edge threshold at 4985.3 eV of a standard $BaTiO_3$ powder. We measured the Ti *K* XAS for powder samples in the transmission mode using two ionization chambers for X-ray detection. The thin films were measured in the fluorescent mode using a 19-element silicon drift detector to avoid self-absorption effects (Figure 2-9) [54].

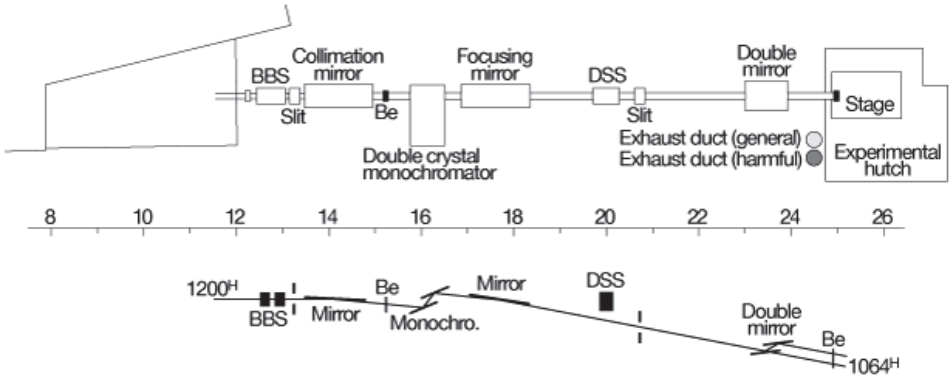


**Figure 2-8.** Beamline layout of BL-9A at the Photon Factory [54].

**Table 2-2**. X-rays available at sample in BL-9A at the Photon Factory [54].

| | |
|---|---|
| Condition | Si (111) focused |
| Energy range | 2.1–15 keV |
| Energy resolution | $\Delta E = 2$ eV, $\Delta E/E =$ ca. $2 \times 10^{-4}$ at 9 keV |
| Photon flux | ca. 4 x 1011 ph/s at 9 keV |

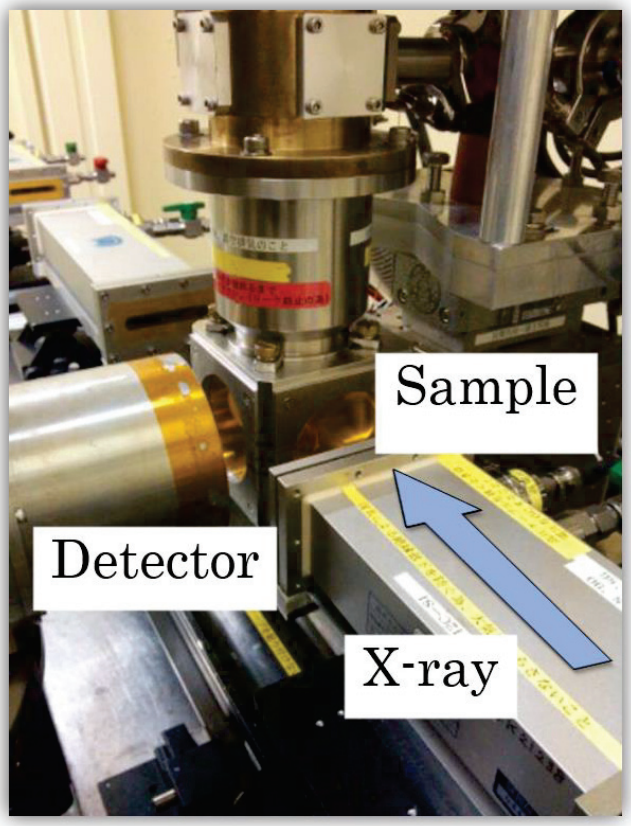


**Figure 2-9.** Schematic view of the experimental setup of the end station of BL-9A at the Photon Factory.

# 3. Results and Discussion

## 3.1. Ti *K*-edge XAS Measurements of STO under Uniaxial Pressure

### 3.1.1. Experimental Setup and Configuration

A 1-mm-thick STO (010) single crystal of 99.99% purity was purchased from Crystal Base Co., Ltd. The sample was cut into pieces 3 × 3 × 1 $mm^3$ in size and set into a uniaxial pressure-load cell. Figure 3-1(a) shows an overview of the cell and (b) shows the experimental configuration during XAS measurements. The sample was sandwiched between a pair of beryllium-copper blocks, and uniaxial pressure was applied on the top *ac*-plane. The magnitude of the applied pressure was monitored using a strain gauge (CFLA-1-350-17, Tokyo Sokki Kenkyujo, Co. Ltd) attached to the beryllium-copper block instead of to the sample itself. During the experiment, the pressure range was maintained at 0.16–0.2 GPa, which is high enough to attain the transition pressure in the pressure-temperature phase diagram [35].

The Ti *K*-edge XAS experiments were performed on the undulator beamline BL39XU at SPring-8. The spectra were measured in the fluorescence mode at temperatures below $T_a$=37K. Linearly polarized X-rays were incident on the $(10\bar{1})$ side of the sample. The full width at half maximum of the cross-section of the incident beam was 9.0 μm (horizontal) × 2.5 μm (vertical), which was much smaller than the surface area of the sample. The polarization vector $E_{hv}$ was converted either to the direction parallel to the pressure axis (*b*-axis) or to the direction parallel to the (*a* + *c*)-axis in the pressurized plane by using a diamond phase retarder. The results of the Brillouin scattering experiment indicated that the dipole moment lies along the (*a* + *c*)-axis. If this

is the case, we can expect an enhancement of the Ti 3*d*-$e_g$ peak in the configuration with $E_{hv}$ parallel to the $(a+c)$-axis.

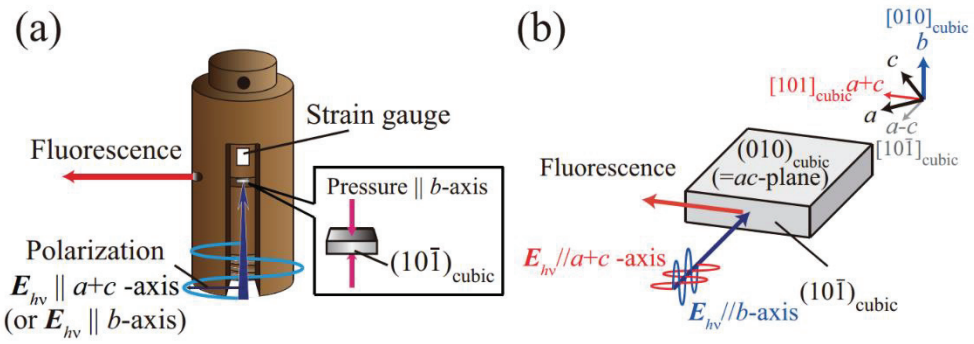


**Figure 3-1**. Schematic of (a) the uniaxial pressure-load cell and (b) the experimental configuration for XAS measurements.

### 3.1.2. Temperature Dependence of Ti *K*-edge XAS Measurements

Figure 3-2 shows a typical Ti *K*-edge absorption spectrum for an STO single crystal measured under uniaxial pressure. The main peak originates from the Ti 1*s*-4*p* dipole transition, while the first two small peaks in the pre-edge region originate from the 1*s*-3*d* quadrupole transition. These two peaks, $e_g$ and $t_{2g}$, are crystal-field-split pairs of 3*d* states [55]. The $e_g$ peak in particular directly reflects Ti-O orbital hybridization. In several Ti oxides with perovskite structures, including STO, the intensity of the $e_g$ peak is enhanced when a Ti atom is located at an off-center site of an oxygen octahedron [16, 56, 57]. We thus focus on the change in the $e_g$ peak to probe the local polarization under uniaxial pressure.

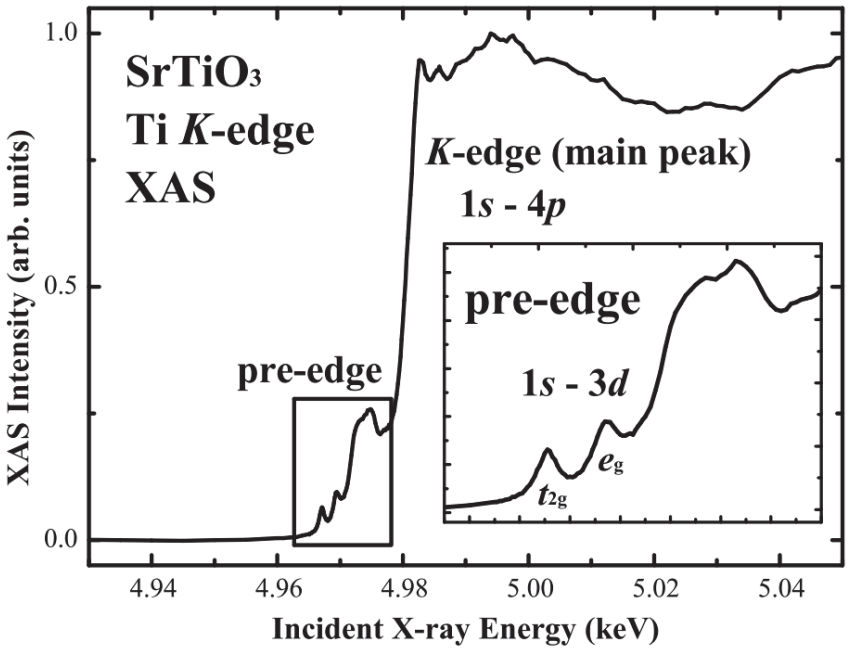


**Figure 3-2**. Ti *K*-edge XAS of an STO single crystal. The pre-edge region is expanded in the inset.

We first consider the temperature dependence of the $e_g$ peak intensity. Figure 3-3(a) shows the Ti *K* pre-edge absorption spectra in the configuration with $E_{hv}$ parallel to the *b*-axis (out-of-plane polarization) under a pressure of 0.16 GPa. If a ferroelectric phase transition is induced by the uniaxial pressure, the $e_g$ peak intensity should be enhanced across $T_a$. At 0.16 GPa, we estimated a transition temperature of 11 K from the pressure-temperature phase diagram in Ref. [35]. However, contrary to our expectation, no marked change was observed around 11 K, as can be seen in the inset, which shows the $e_g$ peak intensity relative to the $t_{2g}$ peak intensity. These spectra were measured in the out-of-plane geometry in order to probe the existence of a local dipole moment along the $[010]_{cubic}$ direction (*b*-axis direction). We concluded that no additional dipole moment was induced along the $[010]_{cubic}$ direction.

The spectra measured under another polarization geometry, with $E_{hv}$ parallel to the (*a*

+ $c$)-axis, are shown in Figure 3-3(b). This configuration is sensitive to a dipole moment along the $[10\bar{1}]_{\text{cubic}}$ direction ([$a$ + $c$]-axis direction) which was predicted. However, these spectra, too, do not show any enhancement of the $e_g$ peak across $T_a$. Although the $e_g/t_{2g}$ intensity ratio shown in the inset does exhibit an enhancement of the $e_g$ peak at $T_a$, a stepwise enhancement at $T_a$ should have been expected. There exists a notable difference in the ratios of the two pre-edge peaks between Figures 3-3(a) and (b). This originates from the angles between the Ti 3$d$ orbitals and the polarization vector of the incident X-rays, and therefore it does not prove the existence of a local dipole moment under uniaxial pressure. From the absence of enhancement of the $e_g$ peak across $T_a$, we can also conclude that uniaxial pressure does not displace the Ti atom from the body center of a $TiO_6$ octahedron. That is, no local dipole moment is induced in STO through the application of uniaxial pressure.

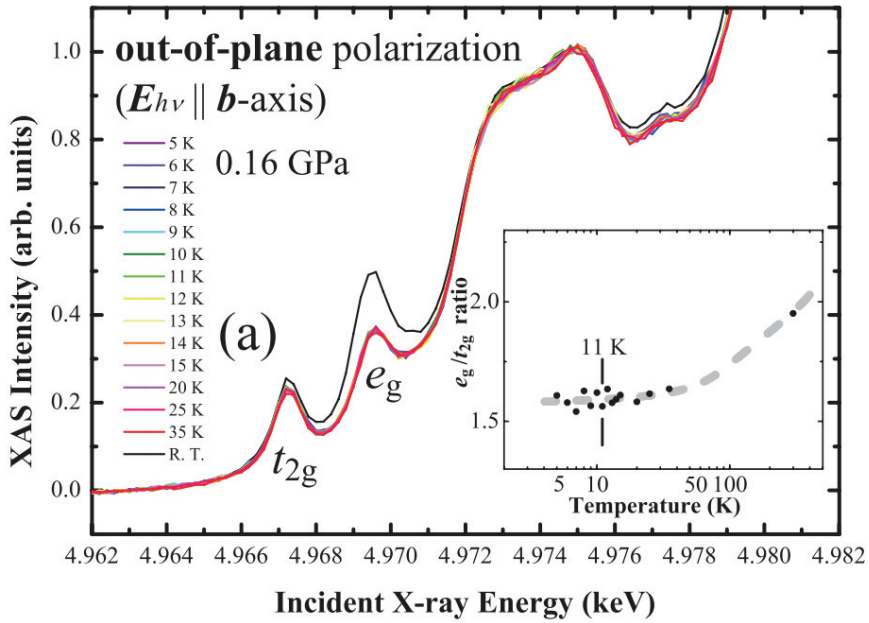

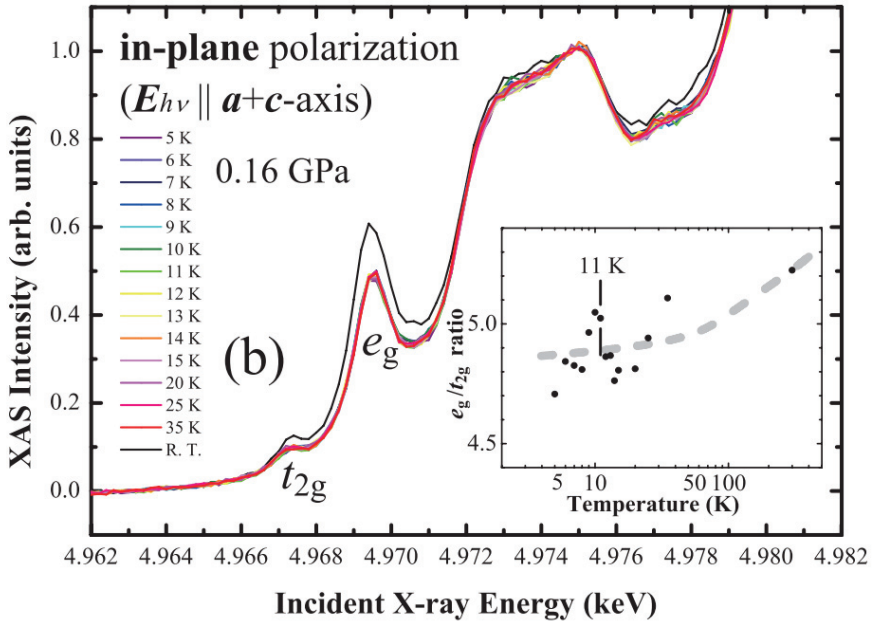


**Figure 3-3**. Ti *K* pre-edge XAS measured under a uniaxial pressure of 0.16 GPa. Each spectrum was measured in (a) the $E_{hv}$ ∥ *b*-axis configuration and (b) the $E_{hv}$ ∥ (*a* + *c*)-axis configuration. Each inset shows the temperature dependence of the intensity ratio of the $e_g$ and $t_{2g}$ peaks. Dashed lines are guides to the eye.

### 3.1.4. Pressure Dependence of Ti *K*-edge XAS Measurements

The pressure dependence of the spectra measured in the out-of-plane polarization geometry is shown in Figure 3-4(a); color differences correspond to different pressures. Lines with circles indicate spectra measured at room temperature. By comparing the spectra measured at room temperature with those obtained at low temperatures, it is clearly observed that the $e_g$ peak decreases in intensity with decreasing temperature. At low temperatures, we also observed a reduction in the $e_g$ peak intensity caused by pressure, together with an energy shift of the peak position. The reduction in the $e_g$ peak intensity with decreasing temperature competes against the enhancement of the dipole

moment caused by the off-centering of the Ti atom. Again, no trace of enhancement can be seen in the inset, which shows the $e_g/t_{2g}$ intensity ratio as a function of pressure.

The $e_g$ peak energy was 4969.40 eV under ambient pressure, and the peak shifts were determined to be 0.16 eV and 0.14 eV under pressures of 0.16 GPa and 0.2 GPa, respectively. In contrast, only a slight shift of the $t_{2g}$ peak was observed, as determined from the Lorentzian fitting of the spectra shown in the lower part of Figure 3-4(a). As a consequence, the energy gap between the $e_g$ and $t_{2g}$ peaks increased with pressure. Similar changes can be seen in the spectra under the polarization geometry with $E_{hv}$ parallel to the ($a$ + $c$)-axis, as shown in Figure 3-4(b). These peak shifts cannot be explained by the anisotropic change in the crystal field that we expect to be induced by uniaxial pressure; if the Ti-O distances along the pressure axis of the $[010]_{cubic}$ direction alone are reduced, the spectra under the two polarization geometries must show differences in the changes of the $e_g$ peak intensity. In our study, however, there was no difference between the two polarization geometries. We thus conclude that under uniaxial pressure at low temperatures, the environment around a Ti atom retains its equivalence, at least between the $[010]_{cubic}$ and $[101]_{cubic}$ directions.

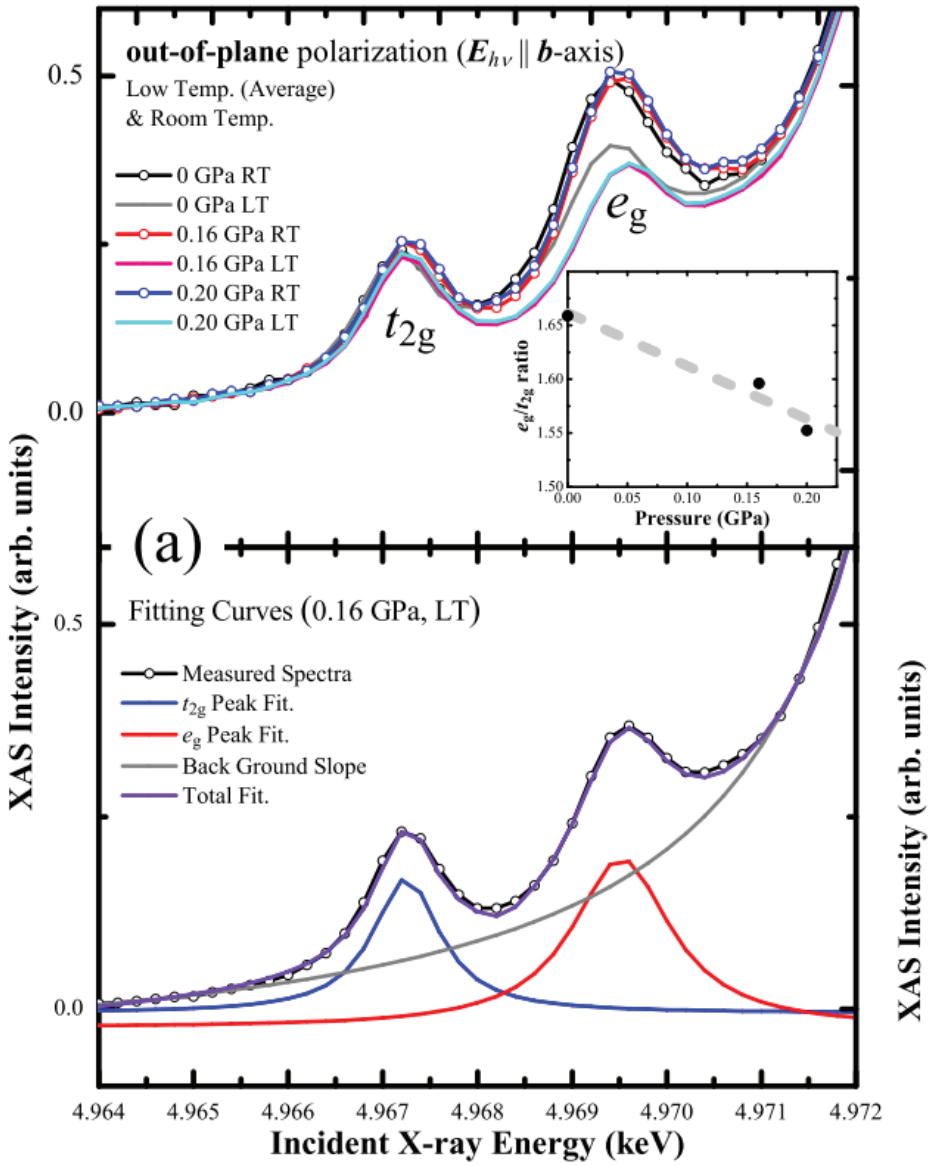
out-of-plane polarization ($E_{h\nu}$ || $b$-axis)
Low Temp. (Average)
& Room Temp.
0 GPa RT
0 GPa LT
0.16 GPa RT
0.16 GPa LT
0.20 GPa RT
0.20 GPa LT
$t_{2g}$
$e_g$
$e_g/t_{2g}$ ratio
Pressure (GPa)
(a)
Fitting Curves (0.16 GPa, LT)
Measured Spectra
$t_{2g}$ Peak Fit.
$e_g$ Peak Fit.
Back Ground Slope
Total Fit.
XAS Intensity (arb. units)
Incident X-ray Energy (keV)

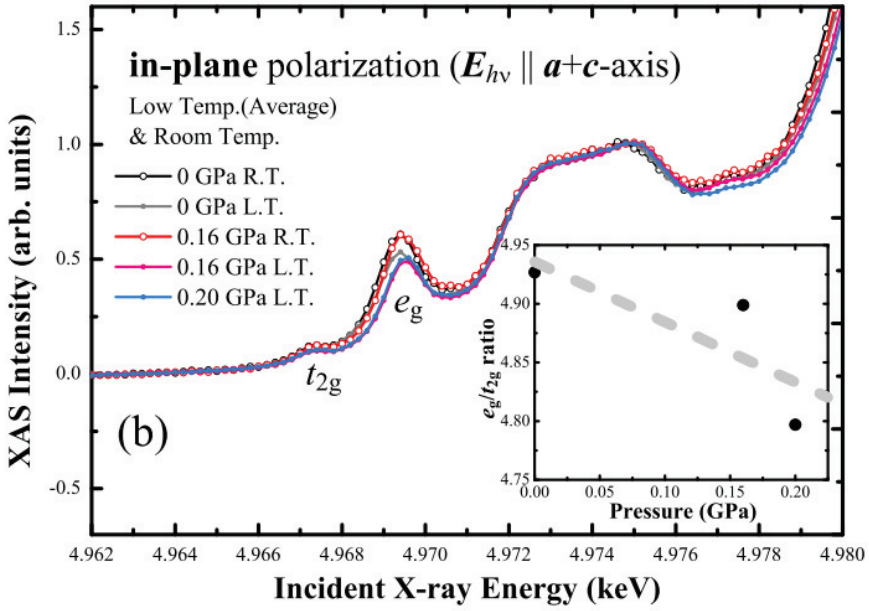


**Figure 3-4**. Pressure dependence of the Ti *K* pre-edge XAS. Each spectrum was measured in (a) the configuration with $E_{hv}$ parallel to the $b$–axis and (b) the configuration with $E_{hv}$ parallel to the ($a$ + $c$)-axis configuration. The bottom half of figure 3-4 (a) shows the result of fitting Lorentzians plus a suitable background slope. Each inset shows the pressure dependence of the intensity ratio of the $e_g$ and $t_{2g}$ peaks. Dashed lines are guides to the eye.

### 3.1.4. Analysis of Local Ferroelectric Order in STO

We propose the following as the mechanism responsible for retaining the equivalence between the coordination environment along the in-plane and out-of-plane directions: the Ti-O bonds shrink equally in both directions under uniaxial pressure, accompanied by a tilt and rotation of the $TiO_6$ octahedra (Figure 3-5), resulting in a reduction of the $e_g$ peak intensity and a peak shift. In order to evaluate the lattice shrinkage, we performed

a naive estimate based on crystal-field theory. From this calculation, we found the shrinkage of the lattice constant to be $\Delta a/a$ = -0.8% at 0.16 GPa. This value is qualitatively reasonable, even though the enhancement of *p–d* hybridization and the deformation from the pseudo-cubic structure are not taken into account. If there is an enhancement of *p–d* hybridization, the intensity of the $e_g$ peak should increase. However, the measured spectra show a decrease in the $e_g$ peak intensity under applied pressure. From this result, we can safely conclude that *p–d* hybridization is not influenced by uniaxial pressure below 0.2 GPa.

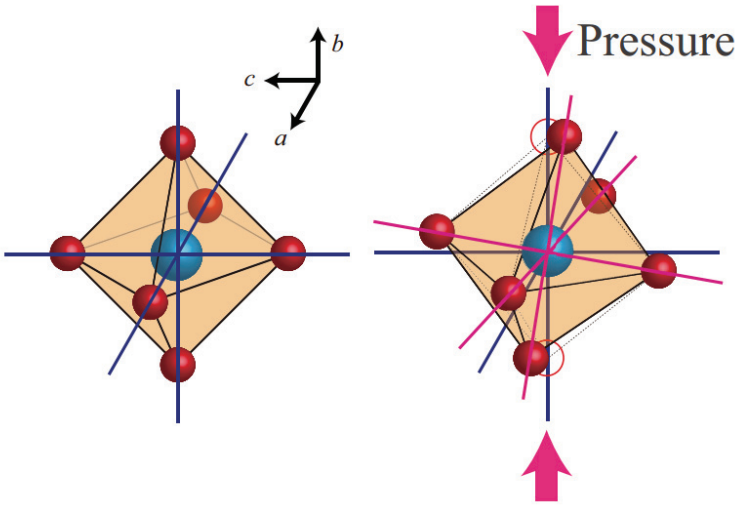


**Figure 3-4**. Schematic views of a $TiO_6$ octahedron under ambient conditions (left) and under uniaxial pressure (right), showing its tilt and rotation under pressure.

Finally, we briefly discuss a further splitting of the crystal-field levels. The uniaxial pressure causes a reduction of the $O_h$ symmetry, which may cause a further splitting of

the pre-edge peaks. In our spectra, however, no such splitting was observed. This clearly implies that any deformation of the unit cell has no serious effect on the pre-edge peaks, at least under a uniaxial pressure of 0.2 GPa.

From the observed result that the $e_g$ peak shows no change in intensity across $T_a$, it is clear that under uniaxial pressure, the Ti atom maintains its equilibrium position at the body center of an oxygen octahedron and that no dipole moment is induced. Therefore, we propose a model in which the $TiO_6$ octahedron tilts and rotates under uniaxial pressure, accompanied by an isotropic shrinkage, without undergoing a ferroelectric transition. Instead, the pressure causes a softening of the Slater mode, accompanied by a ferroelectric transition. In the latter model, neighboring $TiO_6$ octahedra rotate in opposite directions with shrinkage of the unit cell. If a local polarization moment appears in a unit cell due to deformation of the $TiO_6$ octahedron, another local polarization moment appears in the opposite direction in a neighboring unit cell, resulting in short-range ferroelectric order.

## 3.2. Flexoelectricity Measurements on STO Using XAS and RXES

### 3.2.1. Experimental Setup and Configuration

An STO single crystal with dimensions 10 × 3 × 0.2 $mm^3$ and a purity of 4 N was purchased from Crystal Base Co., Ltd. A schematic of the sample holder is shown in Figure 3-5(a), and an enlarged image of the layout of the pressing die showing the definition of the degree of curvature ($\theta_c$) is depicted in Figure 3-5(b). The sample surface was inclined by 30° from the horizontal plane. Both ends of the sample were clamped, and a static stress was applied using a screw through a pressing die. The amount of rotation of the screw controls the degree of curvature of the sample ($\theta_c$). The largest value of $\theta_c$ was estimated to be 1°.

Ti *K*-edge XAS and Ti *Kβ* RXES measurements were performed on beamline BL39XU at SPring-8. The incident X-ray beam was monochromatized using a Si (111) double-crystal monochromator. Vertically polarized X-rays (parallel to the *ac*-plane) were obtained using a 0.1-mm-thick diamond X-ray phase retarder and were irradiated onto the sample. The Ti *K*-edge XAS were obtained in the bulk-sensitive fluorescence mode with a silicon drift detector. The Ti *Kβ* RXES spectra were obtained using a spherical curved Ge (331) analyzer crystal and the two-dimensional hybrid pixel array detector PILATUS. The sample holder was placed in a vacuum chamber to prevent X-ray scattering by air. All measurements were performed at room temperature.

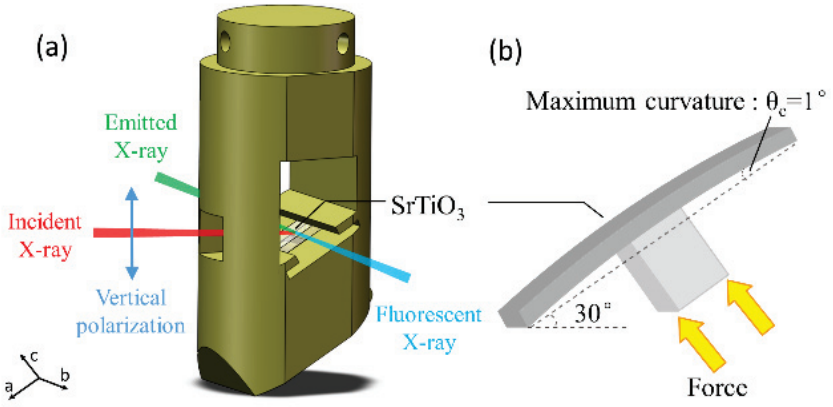


**Figure 3-5** Experimental setup for XAS and RXES measurements on an STO single crystal. (a) Schematic of the experimental holder and X-rays. (b) Layout of pressing die and definition of degree of curvature, $\theta_c$.

### 3.2.2. Angle Dependence of Ti *K*-edge XAS Measurements

Electronic states are important for understanding the physical properties of STO under bending conditions, and XAS is one of several methods that can be used under such conditions. Figure 3-6 shows the Ti *K*-edge XAS of an STO single crystal for various values of $\theta_c$ (0°, 0.33°, 0.67°, 0.83°, and 1°). The spectra are normalized using absorption intensities averaged from 5.02 to 5.05 keV. The spectra can be divided into the pre-edge (inset [a] of Figure 3-6) and post-edge regions. The inset shows a magnified view of the pre-edge region for various $\theta_c$. Here, we are particularly interested in the octahedral coordination of the oxygen atoms around the Ti atom. The pre-edge features are related to the Ti 3*d* states and contain information about the electronic configuration and the local symmetry around the Ti atoms. We observe three

features, labeled A, B, and C in Figure 3-6. Peak A is assigned to the 1s→3*d* ($t_{2g}$) quadrupole transition, whereas peak B is assigned to the 1s→3*d* ($e_g$) quadrupole transition, with both given by an electric quadrupole Hamiltonian with $O_h$ symmetry. The energy separation between peaks A and B directly reflects the crystal-field splitting of the 3*d* orbitals. Figure 3-6 shows that peaks A and B do not appear to depend on $\theta_c$. The relation between the XAS pre-edge peaks and the electronic polarization induced by external conditions has already been discussed by Nozawa *et al.* for STO [18] and by Itie *et al.* for $BaTiO_3$ [58]. In particular, the enhancement of peak B relative to peak A can be explained by the induction of a local ferroelectric moment caused by the relative displacement of the Ti atom excited by external stimuli. From the results of our pre-edge XAS measurements, we observe no such enhancement under bending conditions. The absence of any change in the peak intensity means that a transition into the ferroelectric phase has not been induced by the bending of the STO.

Next, we analyze the pre-edge peak C, main-edge peak D, and the post-edge feature E. Peak C essentially originates from the Ti 1*s*→3*d* dipole transition through Ti 3*d* — O 2*p* hybridization. As $\theta_c$ increases, the intensity of peak C increases; however, the peak remains at the same energy. This can be attributed to an enhancement of the Ti 3*d* — O 2*p* hybridization with increasing $\theta_c$. The main absorption edge D, arising from the 1*s*→4*p* dipole transition, shows no evident changes in either intensity or energy position. Therefore, we can conclude that the Ti valence number is unchanged, regardless of $\theta_c$. In contrast to peak C, the post-edge feature E decreases in intensity with increasing $\theta_c$. Generally, a reduction of crystal symmetry leads to a decrease in the XAS oscillation amplitude due to weakening of the interference by the photoexcited electron. This can be interpreted as indicating the existence of some degree of disorder in the local environment of a Ti atom, particularly in the Ti–O coordination.

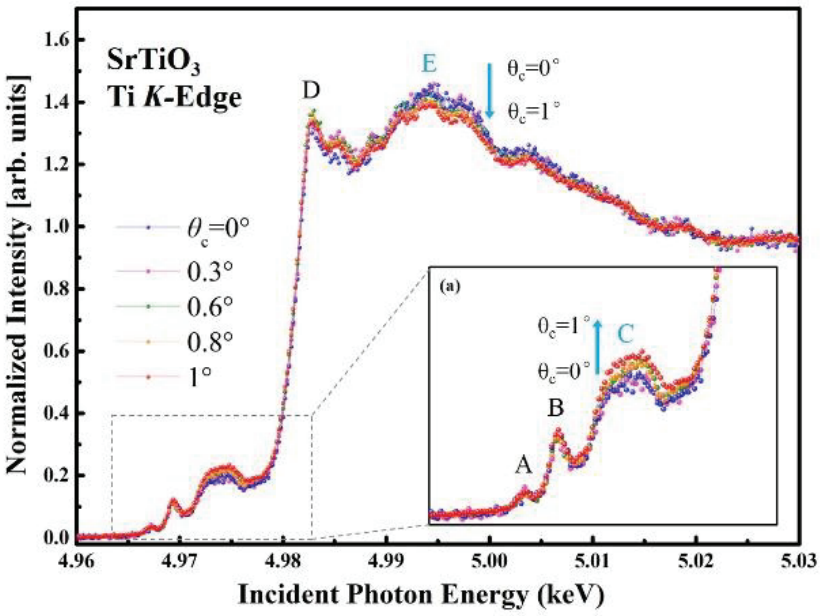


**Figure 3-6** (Color online) Normalized Ti *K*-edge XAS of an STO single crystal at different sample curvatures $\theta_c$. The inset shows the details around the pre-edge region. Arrows indicate the direction of variation of the spectra, from $\theta_c$ = 0° to 1°.

### 3.2.3. FEFF Simulation

To extract detailed information from our spectra, real-space multiple-scattering calculations using the FEFF 8.40 code [59] were performed to elucidate the changes in the local environments of the Ti atoms due to crystal distortions and oxygen vacancies. Figure 3-7(a) compares the XAS spectra obtained for standard and distorted crystal structures. In the standard structure, STO exhibits cubic symmetry (space group *Pm3m*) with the lattice parameter $a$ ( = $b$ = $c$) = 3.9050 Å. Crystal distortions are incorporated by changing the lattice parameter $c$, while fixing the lattice parameter $b$ and the unit-cell volume, for tensile strains up to $\Delta c/c$ = 1.3%. As shown in Figure 3-7(a), the crystal distortion expected from bending has little effect on the spectrum, except for the

post-edge feature at 4.998 keV, which shows a slight reduction in intensity. This trend is consistent with the observed reduction of intensity of peak E in the experimental spectra shown in Figure 3-6.

We also performed a calculation for an oxygen-vacancy model. Charged oxygen vacancies may be introduced during the growth and processing of oxide single crystals. Furthermore, it has been proposed that crystal distortion may contribute to the formation of oxygen vacancies [60]. Consequently, we assume that bending may also introduce oxygen vacancies into an STO crystal. Changes in local structure can also be attributed to various types of oxygen vacancies, with the electronic-configuration changes occurring on the scale of several atomic spacings. Here, we model the influence of nearest-neighbor oxygen vacancies (first coordination shell) by removing one oxygen atom from the $TiO_6$ octahedron. The calculated XAS spectra for STO in the standard and oxygen-vacancy conditions are compared in Figure 3-7(b). In contrast to the effect of distortion, a clear enhancement appears in the pre-edge region of the spectrum due to an oxygen vacancy.

Based on our simulations, we find that the effects of FxE in STO arise predominantly from two sources: crystal distortions and oxygen vacancies. The observed effects are likely to be a combination of both factors, as indicated by Figure 3-7(c), which shows the simulated XAS spectra for STO with curves representing the spectra for gradually varying conditions. To test this prediction, we implemented certain conditions in the XAS simulations. Initially, we fixed the total number of STO unit cells at 30. All unit cells have standard lattice parameters in the absence of bending stress. At the first stage of bending, we incorporate crystal distortion into the lattice by increasing $\Delta c/c$. With further increase of the bending stress, oxygen vacancies gradually emerge, together with a continuing increase of $\Delta c/c$. We naively modeled this condition by increasing the relative ratio of the number of oxygen-defect unit cells to the number of distorted unit cells within the fixed number of 30 unit cells. In Figure 3-7(c), the ratio of oxygen vacancies to crystal distortion increases from 1:29 to 4:26. Significantly, we observed

that the features of the pre- and post-edge peaks vary monotonically with increasing crystal distortion and increasing oxygen vacancies (as indicated by the arrows in Figure 3-7[c]). Thus, the simulation satisfactorily reproduces the trends observed for the dependence of the experimental STO spectra on the bending angle. As the incorporation of crystal distortions and oxygen vacancies into the structure shows an effect that is essentially identical to the experimentally observed trends, we conclude that an appropriate combination of crystal distortions and oxygen vacancies is present in the experimental samples.

It should be mentioned that the two factors, crystal distortions and oxygen vacancies, are correlated with each other. The bending stress induces a reduction of the local symmetry, which directly leads to anisotropic Ti-O bonding. The more the crystal is distorted, the more Ti-O bonding becomes anisotropic. Hence, oxygen vacancies are increasingly created by the bending stress.

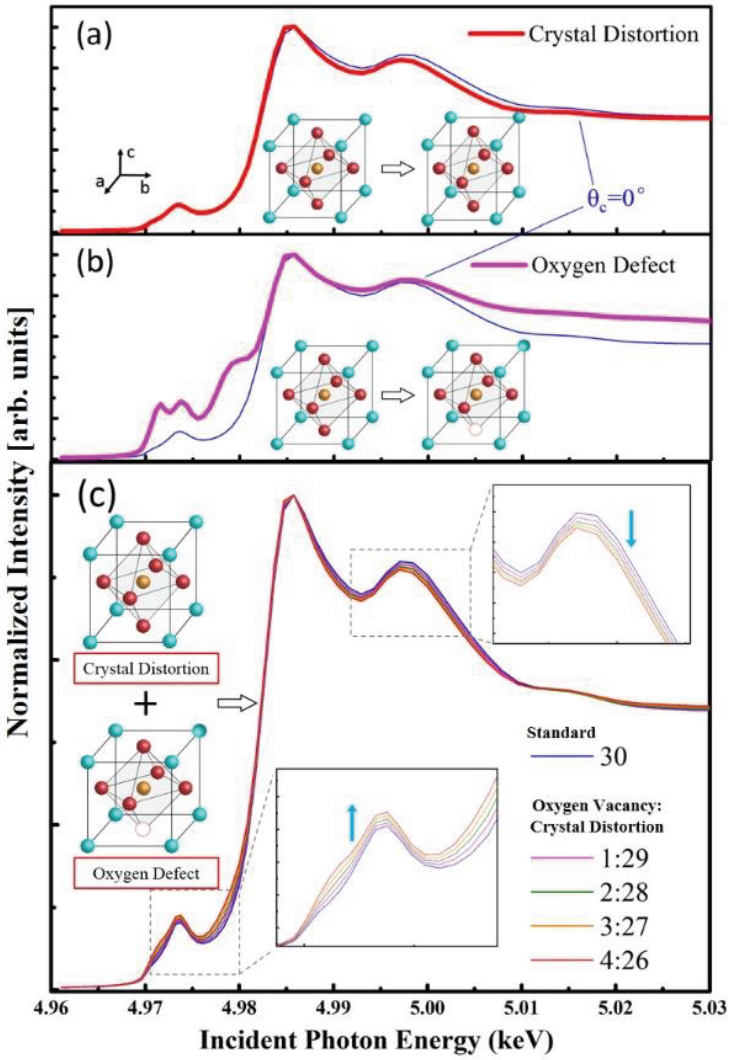


**Figure 3-7** Theoretical calculations of Ti *K*-edge XAS of STO for various structural models, performed with the FEFF 8.40 code. (a) Comparison between simulated spectra in standard and distorted conditions. (b) Comparison between simulated spectra in standard and oxygen-defect conditions. (c) Simulated XAS spectra of STO that combine the effects of crystal distortions and oxygen vacancies. The insets show curves representing spectra for gradually varying conditions.

### 3.2.2. Angle Dependence of Ti $K\beta$ RXES Measurements

To test the conclusions extracted from the XAS spectra, we measured the Ti $K\beta$ RXES spectra with special attention paid to the tiny charge-transfer (CT) excitation peaks that appear between the intense elastic peak and the $K\beta_{2,5}$ (Ti $3d$ + O $2p$ → Ti $1s$) transition. Figure 3-8 shows a magnified view of the two CT peaks, with a constant vertical offset for values of the degree of curvature $\theta_c$ varying from 0° to 1°. The photon excitation energy, which is equal to the elastic peak energy, was tuned to the main-edge jump D in the XAS spectrum. The transferred energy, i.e., the energy separation from the elastic peak, was chosen as the abscissa. As shown in Figure 3-8, two CT peaks are observed at 15 eV (CT1) and 7–8 eV (CT2). These peaks occur in both STO and $BaTiO_3$ spectra, and their origin have been theoretically elucidated based on the $TiO_6$ cluster model. The most important conclusion is that the CT2 peak is directly related to the off-centering of the Ti atom in its oxygen octahedron. In brief, the CT2 peak is an appropriate fingerprint of the local polarization; while it is absent in a perfect cubic environment, its intensity increases and shifts toward the lower-energy-transfer side with increasing local polarization (either spontaneous or induced).

Further analysis of Figure 3-8 shows that with increasing $\theta_c$, the CT2 peak remains at a fixed energy but slightly decreases in intensity; i.e., the representative peak amplitudes are $a_0 \geq a_1 \geq a_2 \geq a_3 \geq a_4$. The CT2 peak exists even in the cubic phase with no bending ($\theta_c = 0°$), implying that a local permanent polarization is present in our original sample. Since the thin-plate sample was prepared by microcutting followed by long-term polishing, the local polarization exists due to oxygen anion defects. A reoxidation treatment was performed by the sample provider; however, we employed a surface-sensitive configuration for fluorescence X-ray detection (Figure 3-5), finding a negligible effect on the spectra. Nevertheless, we find that bending induced neither an additional enhancement of the local polarization nor the development of ferroelectric order. Instead, based on the discrete profile of CT2 at $\theta_c$ = 1°, we conclude that a

random distribution of local polarizations, with various orientations and magnitudes, exists in the sample, indicating the presence of oxygen defects introduced by the bending stress. According to the $TiO_6$-cluster model results, the CT2 profile becomes more distinct if the crystal distortion becomes measurable due to bending. From the RXES results, we can also conclude that the oxygen defects may play a major role in the spectral changes due to bending; this is in accordance with the XAS results.

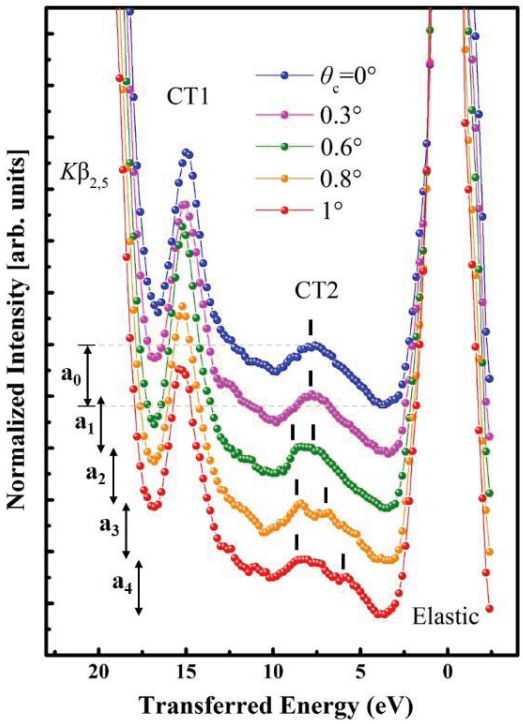


**Figure 3-8** Ti *Kβ* RXES spectra between the elastic and $K\beta_{2,5}$ peaks, showing the dependence of the CT peaks on the degree of curvature, $\theta_c$ = 0°, 0.3°, 0.6°, 0.8°, and 1°, at room temperature. The excitation X-ray energy was 4.983 keV.

Before summarizing this study, it is instructive to discuss recent reports concerning

the polarization induced at the surfaces or interfaces of thin films. In 2007, Woicik *et al*. reported ferroelectric distortion in STO thin films grown on Si (001) and concluded that the compressive biaxial strain achieved by coherent epitaxial growth is essential for this phenomenon [40]. Recently, a theoretical prediction also concluded that there are unavoidable surface contributions to the flexoelectric effect. Obviously, it is much easier to introduce a strain gradient in thin films rather than in a single crystal, and therefore we can expect an apparent crystal-distortion effect. A follow-up study with various types of thin films is underway.

## 3.3. X-ray Spectroscopic Evidence for Ferroelectricity in STO Thin Films

### 3.3.1. Sample Preparation

We purchased from the TOSHIMA Manufacturing Co., Ltd, 100-nm-thick STO thin films that had been deposited on various substrates (MgO, $LaAlO_3$, $SiO_2$, and glass) by the sputtering technique. They were prepared by annealing the as-deposited films at 600℃ to obtain high-quality crystal structures. We also bought from Kojundo Chemical Lab. Co., Ltd, standard powder samples of $ATiO_3$ (where A = Ca, Sr, Ba, or Pd) as references.

### 3.3.2. Detection by XRD and EXAFS

Figure 3-9 shows the $\theta$–$2\theta$ XRD scan patterns for STO films on MgO/$LaAlO_3$ (LAO)/$SiO_2$/glass substrates. According to a previous report [38], there are no diffraction peaks in the XRD patterns of amorphous films, indicating the absence of crystallinity. However, our measurements show that the diffraction peaks of the STO thin films (Figure 3-9 shows only the film on a glass substrate) exhibit good agreement with those of standard STO powders.

In the crystallized STO thin films, there is no evident preferential orientation, which is the same as for epitaxial thin films. The index of the above XRD patterns are determined and marked, which indicates that there is no detectable secondary phase emerging in the STO films. The inset of Figure 3-9 shows the comparative results of high-resolution XRD curves in the region from $2\theta$ = 31.8° to 33.0° for STO films on

different substrates. The rank of lattice constants is $SiO_2$ ≫ MgO ＞ STO powders ＞ LAO, and the glass substrate provides an amorphous surface without a definite lattice parameter. The (110) positions of the films on $SiO_2$ and glass are similar to that of a standard STO powder. In contrast, the (110) diffraction angle of the STO film on LAO shifts to lower energy, while that of the STO film on MgO shifts to higher energy, suggesting the existence of compressive strain and tensile strain, respectively.

Figure 3-10 shows the magnitudes of the Fourier Transforms of the $k^3$-weighted EXAFS oscillation signals for the various STO thin films and standard powders plotted as functions of the radial distribution function relative to center Ti atom. The first coordination shell (which peaks at about 1.4 Å) and the second-neighbor shell (peaking at about 3.1 Å) are attributed to the Ti-O and Ti-Ti bonds, respectively, of the local structure in STO. As expected from the XRD results, patterns for the STO films and powders are nearly identical, confirming that the STO films indeed remain crystalline like the powders, retaining a long-range lattice structure. In contrast, for amorphous films, only the peak of the first coordination shell exists, indicating that the $TiO_6$ octahedra remain intact but without forming a periodic correlation. The decrease in intensity of the peaks for films relative to those for powders is just a consequence of the bond-length disorder caused by the off-center displacement of the Ti atoms. This means that the symmetry is indeed broken, as expected for a ferroelectric transition. To make a concrete verification of the local electronic structure distortions, resulting in the formation of a polar state, we need to measure and analyze the pre-edge regions of the XAFS.

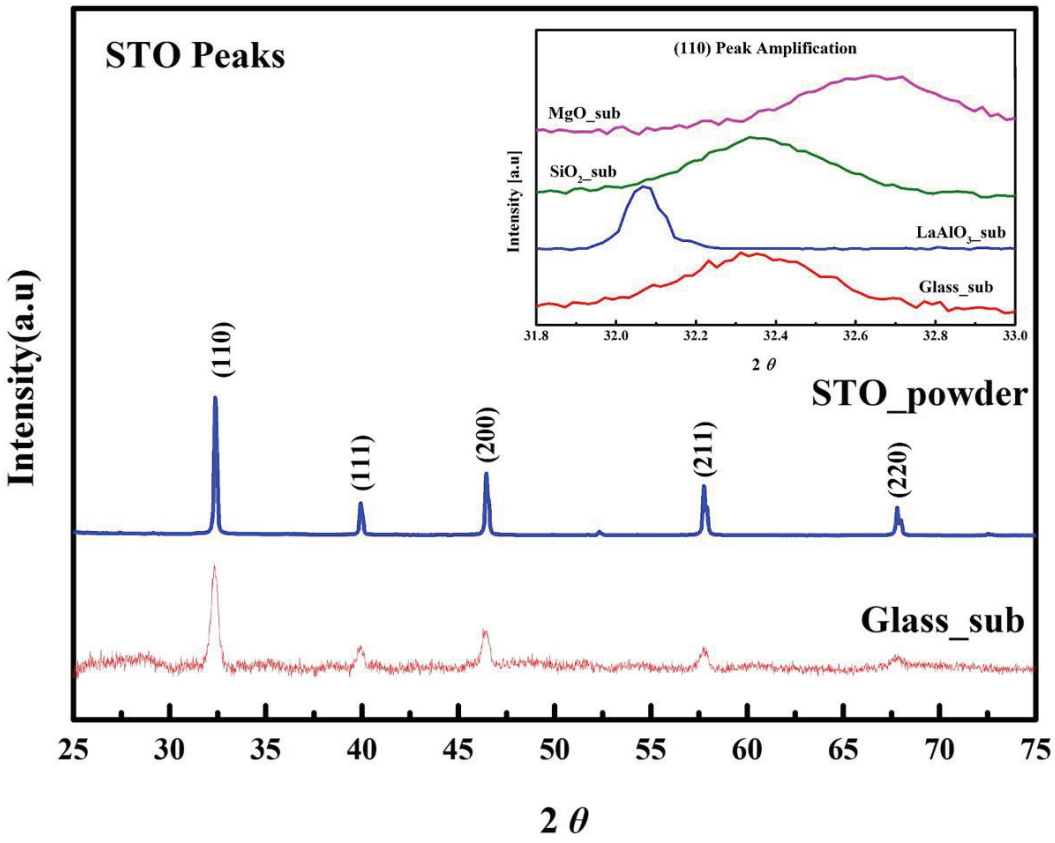


**Figure 3-9** XRD patterns of STO films on glass substrates and of standard STO powders. The inset displays an enlargement of the diffraction peaks in the 2$\theta$ interval 31.8°–33.0°, which shows the position and shape of the (110) peaks for different films.

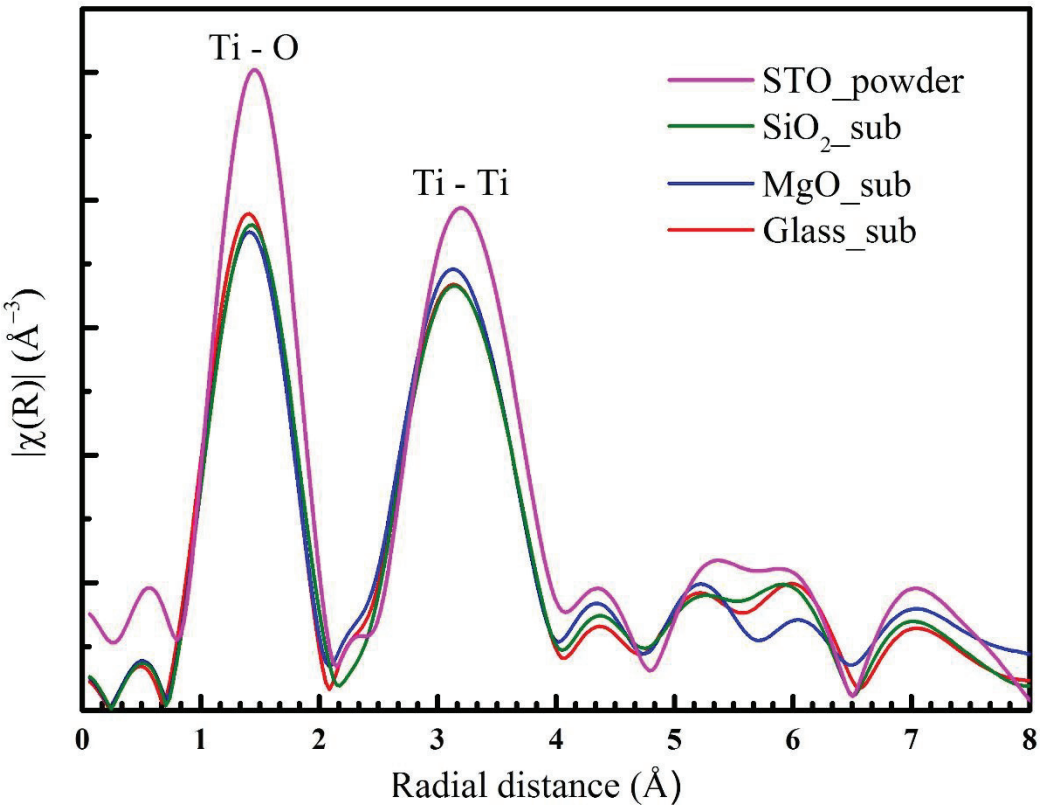


**Figure 3-10** Fourier Transform magnitudes for STO thin films on different substrates compared with that for a standard STO powder.

### 3.3.3. Ti *K*-edge XAS Measurements for STO Thin Films

Figure 3-11 presents the Ti *K*-edge XANES spectra, comparing the results for STO thin films on glass substrates and in powder form. In addition, we obtained for reference the corresponding spectra for $CaTiO_3$, $BaTiO_3$, and $PbTiO_3$ powder samples at room temperature. The spectra are normalized by equalizing the edge jumps. Reviewed from the viewpoint of selection rules, these Ti *K*-edge XANES spectra have a strong relationship to the Ti $1s \rightarrow 4p$ transition hybridized with Ti $3d$ and O $2p$ orbitals, and the density of the unoccupied Ti $4p$ states makes the main contribution to the feature.

The pre-edge features are related to the Ti 3*d* orbitals and contain information about the local electronic structure and the symmetry of coordination around the Ti atoms [61]. The transition of a 1*s* electron to a 3*d* orbital provides the electric quadrupole and dipole components in each of the displayed $ATiO_3$ measurements. As shown in the STO spectra, the two peaks A and B are the quadrupole transitions of the Ti 1*s* electrons to the Ti 3*d* orbitals. The latter are attributed to the $t_{2g}$ ($d_{xy}$, $d_{yz}$, and $d_{zx}$) and $e_g$ ($d_{3z^2-r^2}$ and $d_{x^2-y^2}$) unoccupied states, the difference of which are the results of the crystal-field splitting. Peak C is an electric dipole transition derived from the Ti 1*s* state 3*d* hybridized with the O 2*p* state. The $e_g$ peak can provide information about the distortion of the Ti atom position, with the peak intensity proportional to the mean square of the Ti off-center displacement. This results in a short apical Ti-O bond illustrating ferroelectricity. The *K*-edge XANES of the $ATiO_3$ powder samples exhibit evident enhancements of the $e_g$ peak, from bottom to top in Figure 3-11, supporting this conclusion.

The specific differences between the STO film and powder can be seen in insets (i) and (ii) of Figure 3-11. First, we find a remarkable enhancement of the $e_g$ peak for the STO film as compared with that for the powder sample. This change in the pre-edge peak intensity means that a local transition into a ferroelectric phase has been induced in the STO thin film. It is also noticeable that the intensity ratio of the $t_{2g}$ and $e_g$ peaks for the STO thin film is analogous to that for the $BaTiO_3$ powder sample, validating the conclusion that the Ti atom is off-center. Conversely, the main absorption-edge peaks show no difference in either intensity or energy position, which suggests that the Ti retains its standard valence of $Ti^{+4}$, in a $d^0$ configuration, in the STO film. In contrast to feature B, feature D of the oscillations above the absorption edge decreases in intensity compared to the powder sample. This is due to the symmetry reduction caused by the weakening of interference by the photoexcited electron. Consequently, we conclude that structural distortions exist in the local arrangement of atoms around the Ti atoms, particularly in the Ti–O coordination ($TiO_6$ octahedra). These characteristics of XAS are absent from the amorphous STO thin films. From the resemblance of its spectroscopic

characteristics to the powder sample, we find that the thin film shows good crystalline order, which is echoed in both the X-ray diffraction and EXAFS measurements.

To understand the mismatch effect and local structural distortions among our four different types of thin films, we explored the spectral modifications of the Ti *K* edge XAS. Comparing the full spectra of STO thin films on different substrates, we can see no obvious signs of change; it is necessary to examine the enlarged parts of the pre-edge and main-edge regions, which are shown in Figure 3-12 and Figure 3-13, respectively, to see that the local atomic environments of the Ti atoms in STO are not much altered by different mismatch effects. From Figure 3-12, peaks B1 and B2 are assigned to the spectral components $t_{2g}$ and $e_g$, respectively, and the separations of the two peaks vary with the STO films on different substrates. The $t_{2g}$ feature is clearer and sharper in films on LAO and MgO than it is for other substrates. In addition, the position of the $t_{2g}$ peak is associated with the grain size of the thin film, which is consistent with the above-mentioned results of our XRD measurements. Figure 3-13 shows that the STO thin films grown on LAO and MgO are also accompanied by an enhancement of the main absorption edge. This indicates that these changes are not only due to the off-center displacement of the Ti atoms but also that they are affected by lattice distortions induced by the mismatch effect.

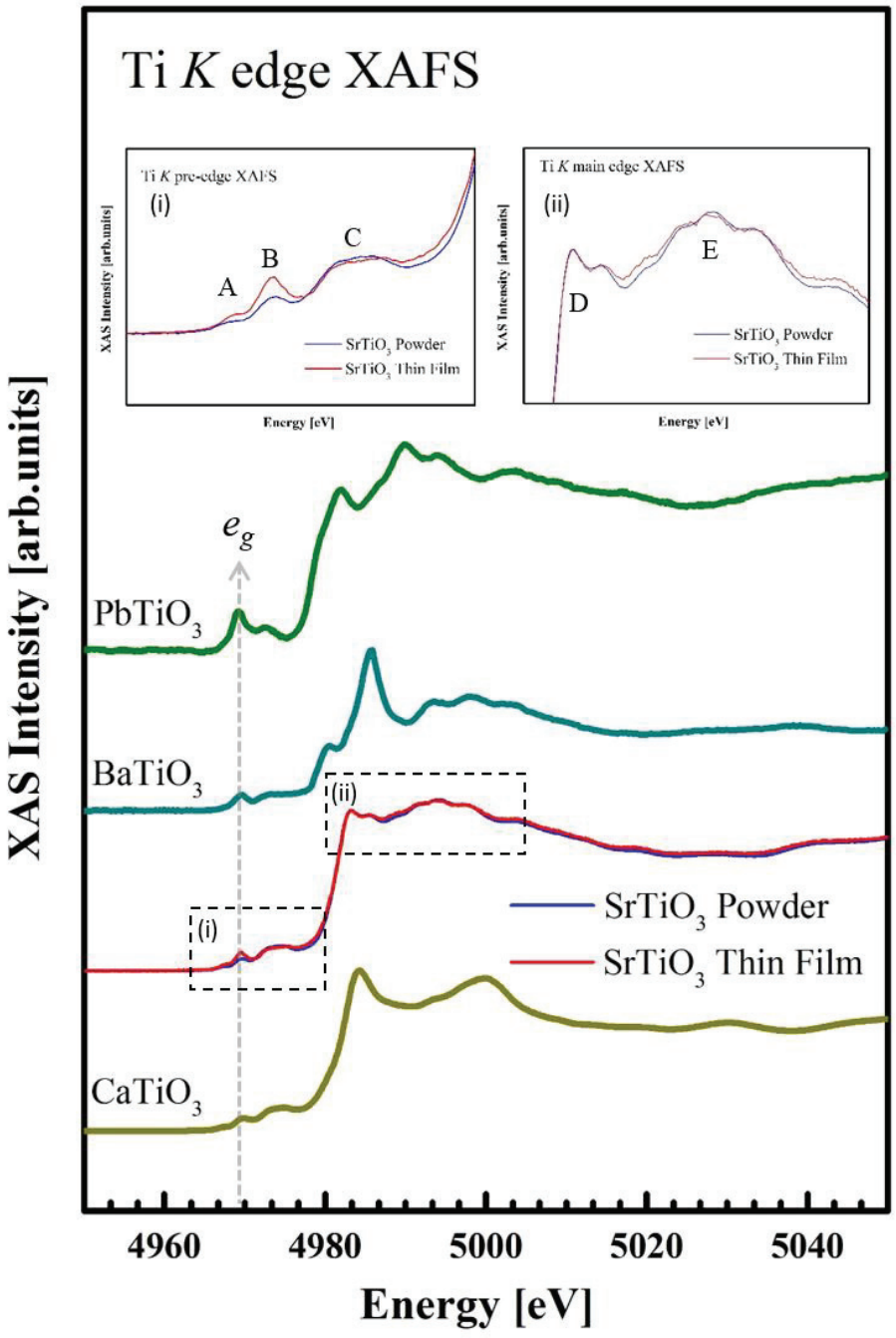


**Figure 3-11** Ti *K*-edge XAFS for the STO thin film and for bulk samples of STO, $PbTiO_3$, $BaTiO_3$, and $CaTiO_3$. Inset (i) is a magnification of the pre-edge region of the STO thin film and powder. Inset (ii) is a magnification of the main-edge region.

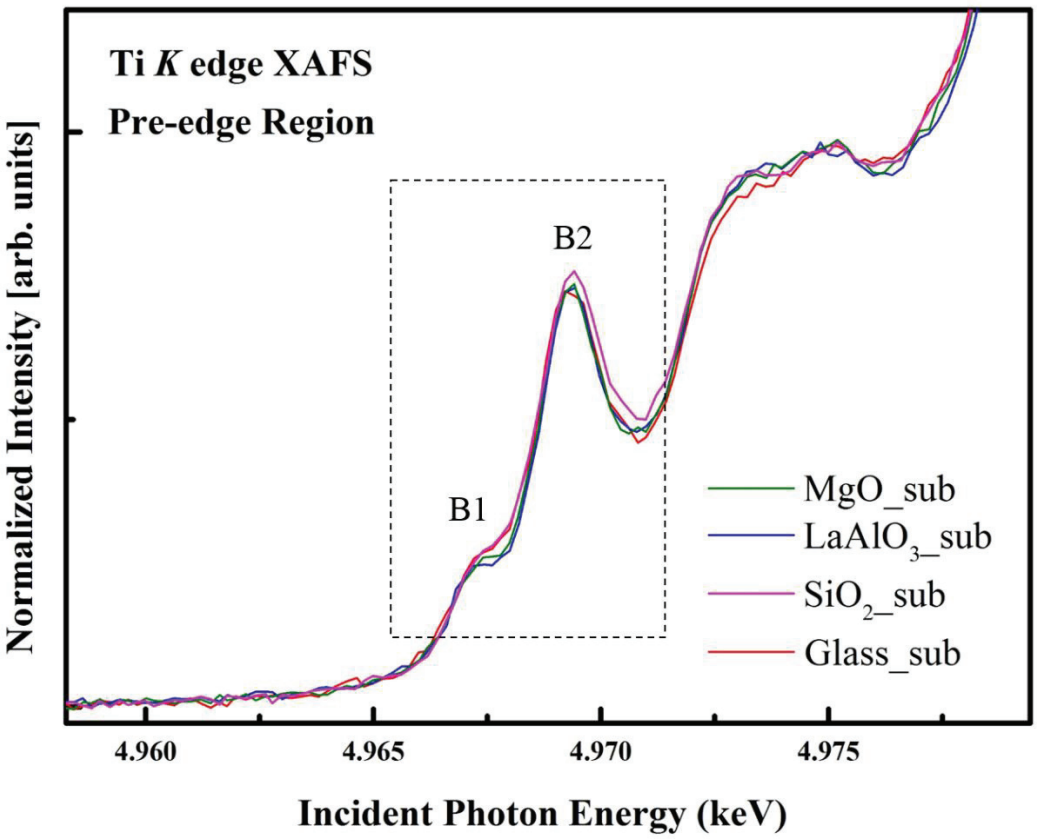


**Figure 3-12** Pre-edge region of STO films on different substrates.

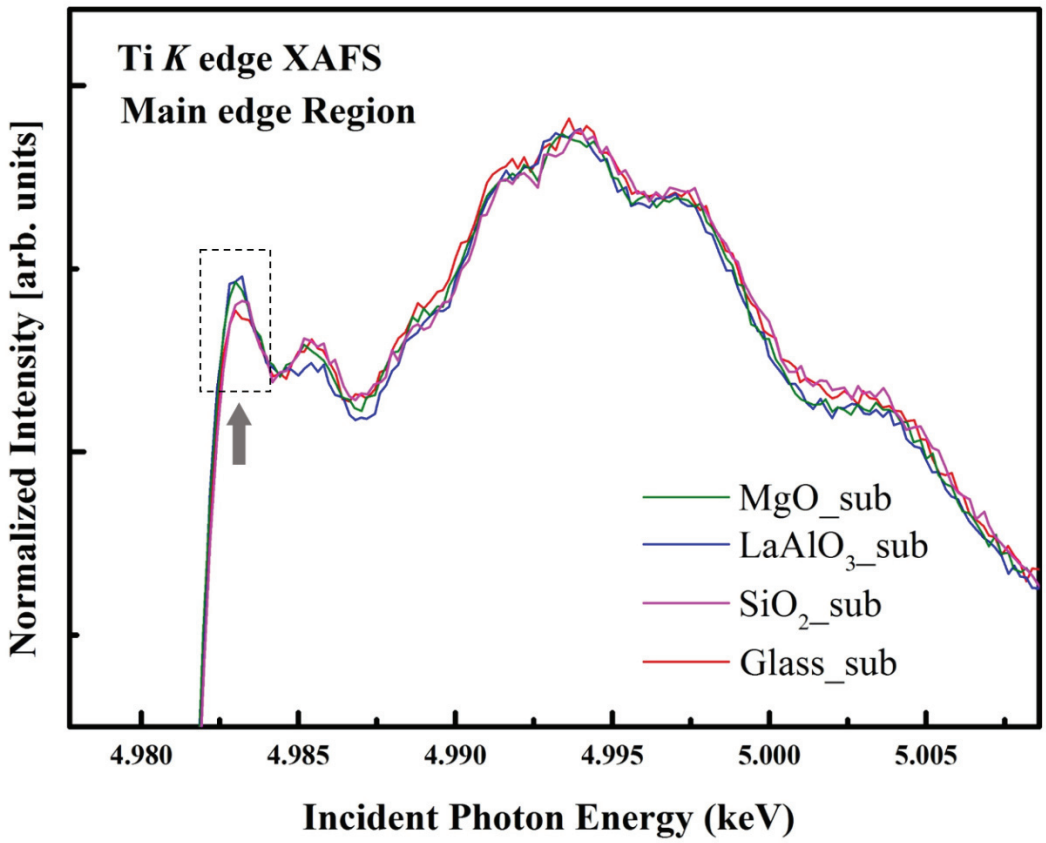


**Figure 3-13** Main-edge region of STO films on different substrates.

### 3.3.4. FDMNES Calculation

To investigate further the nature of the local structural distortions indicated by our spectra, we constructed a model using the FDMNES routine, which uses a real-space, X-ray-absorption, finite-difference calculation. To reproduce the experimental STO XANES features, we applied a self-consistent treatment of the ground and excited states, including quadrupole contributions and optional Hubbard corrections U, which are necessary to localize the corresponding states. The parameter settings correspond to different degrees of the $TiO_6$ rotation (denoted by $u$ = 0.25, 0.24, 0.23, and 0.22 in the

figure legend). The extent of the AFD rotation and the very tiny 0.01 Å Ti off-center displacement are treated as fixed parameters in the calculations. The model calculations assumed a radius $r$ = 7.2 Å in real space for all the electrons, according to the symmetry requirements of the space group I4/*mcm*, which treats the impact of neighboring atoms on the electronic states separately. Figure 3-14 displays the simulated spectra corresponding to structural distortions of the STO films, given the presence of off-center Ti atoms, FE, and AFD $TiO_6$ rotations, which are important for interpreting the slight differences in the XAS. The calculations show that both the first two peaks in the pre-edge structure and the main-peak features tend to strengthen in intensity with increasing degree of $TiO_6$ distortion, for a fixed Ti displacement. Together with the experimental results, the calculations lead us to speculate that the STO thin films on both LAO and MgO substrates undergo increasing rotation, retarding the reduction of symmetry induced by the off-center Ti displacement. Therefore, the simulation results satisfactorily reproduce the trends observed for the experimental STO spectra on different substrates. We consider that the coexistence and competition between FE and AFD within the STO thin films provides the explanation for the FE and AFD effects, in agreement with the experimentally observed trends, especially for the samples including the mismatch effect [62, 63].

To associate the spectral variations we observed with the dependence on $TiO_6$ rotation and off-center Ti positions found by FDMNES, we calculated the partial density of states (DOS) from the spectra in the vicinity of the Fermi level based on the above simulations [64, 65]. In panels (i) and (ii) of Figure 3-15, we show comparisons among the calculated DOS of Ti 3*d* and O 2*p* between 0 and 15 eV above the Fermi level. Peaks C1 and C2, corresponding to the transitions $t_{2g}$ and $e_g$, have a strong relationship with the DOS of Ti 3*d* and O 2*p*. For the Ti 3*d* DOS contributions, peak C1, near 5.4 eV, shows a gradually increasing dependence on the degree of rotation, whereas peak C2, near 6.0 eV, exhibits the opposite trend. Moreover, the great similarity between the above DOS distributions can also be observed in the D1 and D2 features of the O 2*p*

DOS. We note that the unoccupied part of the DOS follows the same tendency as our observation of the pre-edge peak of the XANES spectra of STO thin films. This behavior supports the interpretation of these structures as being associated with the hybridization of the Ti 3*d* and O2*p* DOS.

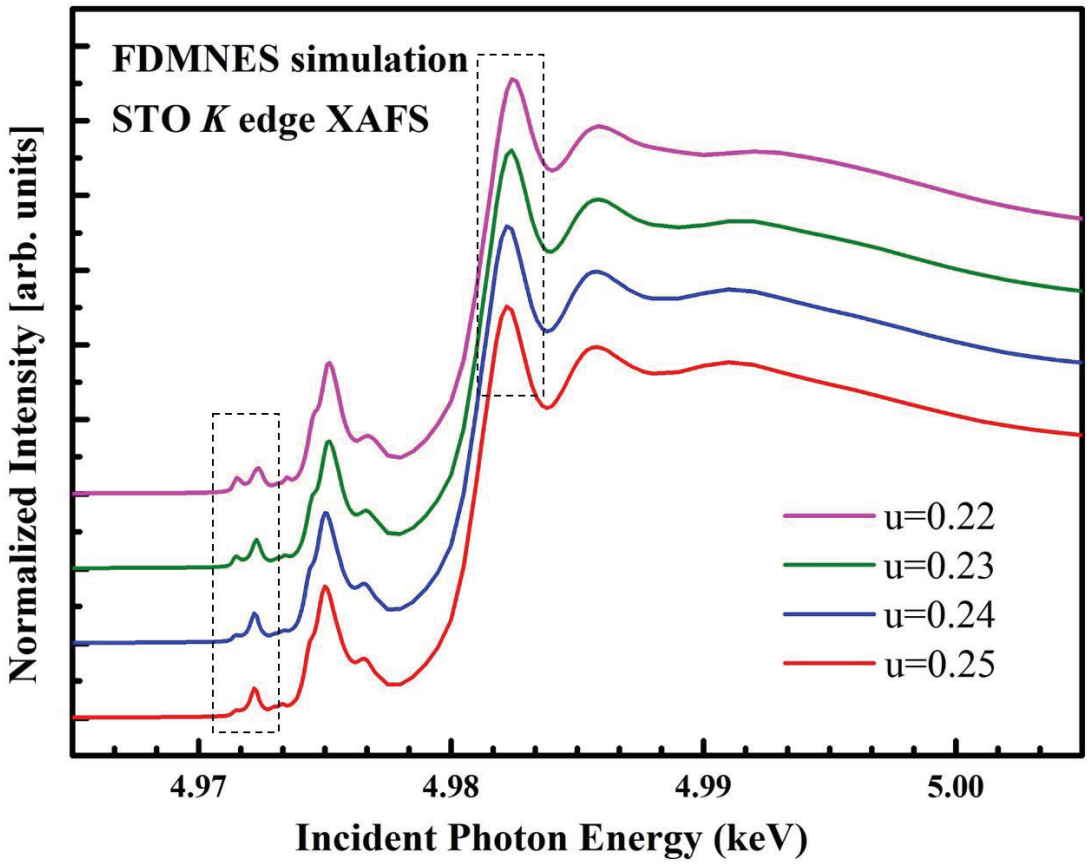


**Figure 3-14** Self-consistent calculation of Ti *K*-edge XAFS for STO, given a constant Ti off-center displacement, together with various $TiO_6$ rotation structural models, performed using the FDMNES code.

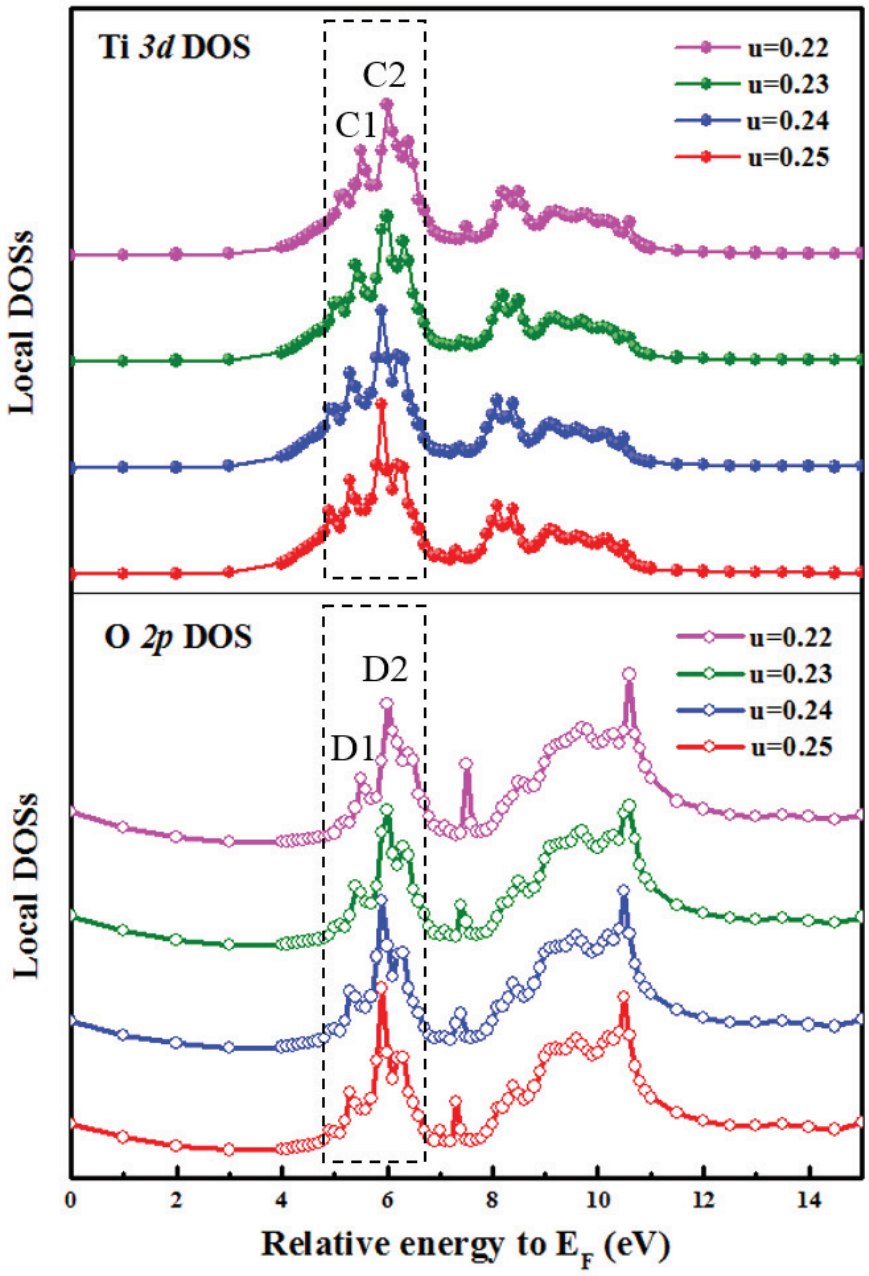


**Figure 3-15** Calculated partial phonon density of states for the Ti 3*d* state and the O 2*p* state.

Before concluding, we briefly address other possible origins of the order parameter

for ferroelectric polarization in STO thin films. Flexoelectricity, as spontaneous polarization induced by a strain gradient, is likely to be introduced at an interface by the lattice mismatch between an STO thin film and the substrate. Our previous work has revealed the absence of the flexoelectric effect in STO single crystals caused by bending. Nonetheless, an STO thin film has the potential to be used to generate and modulate flexoelectricity, which may play a role in our samples [66]. Another candidate for spontaneous polarized order in our samples may be the decreasing grain sizes in STO thin films. From our XRD and EXAFS experimental results, we observed a granular structure of an STO thin film analogous to that of STO nanoparticles, which have been found to exhibit possible ferroelectricity at room temperature. For $BaTiO_3$ nanoparticles, the crystal structure changes from tetragonal to cubic with reducing particle size. However, for the cubic STO nanoparticles, tetragonal distortion will occur and may contribute to the polar structural state [67].

# 4. Conclusion

In the present research, we examined the origin of local ferroelectric order in a pure STO single crystal and in thin films caused by external pressure and structural deformations using the technique of X-ray spectroscopy with synchrotron radiation. The results can be summarized as follows:

**Local ferroelectric order induced by uniaxial pressure**

We performed X-ray absorption spectroscopic measurements under uniaxial pressure parallel to the *b*-axis at the Ti *K*-edge of an STO single crystal. Since the Ti 3*d* $e_g$ peak directly reflects the displacement of a Ti atom from the body-centered site of a $TiO_6$ octahedron, we expected to observe an enhancement of the $e_g$ peak across the ferroelectric phase transition.

In contrast to our expectation, however, no enhancement was observed. At low temperatures, the pre-edge peaks show energy shifts due to uniaxial pressure, which was observed in measurements with $E_{hv}$ parallel to both the *b*-axis and the (*a* + *c*)-axis. This indicates that the environment around a Ti atom retains its equivalence, at least between these two directions, under uniaxial pressure at low temperatures. Therefore, we proposed a model of tilt-and-rotation of a $TiO_6$ octahedron as a mechanism to maintain the equivalence between the coordination environment along the in-plane and out-of-plane directions. In this model, ferroelectric order cannot exist because neighboring $TiO_6$ octahedrons rotate in opposite directions. The tilt-and-rotation of a $TiO_6$ octahedron can explain the fact that no evidence for a ferroelectric phase transition was observed in the Ti-*K* pre-edge XAS.

**Local ferroelectric order induced by bending pressure**

We also measured the dependence of the Ti *K*-edge XAS and RXES spectra on the degree of curvature ($\theta_c$) of an STO single crystal in order to investigate the local origin of FxE. Both the pre-edge quadrupole peaks in the XAS and the CT peaks in the RXES show little $\theta_c$ dependence, which clearly indicates no off-centering of the Ti atoms. In other words, bending does not induce a displacive-type ferroelectric transition. The FEFF simulations we carried out indicate that the FxE reported so far for STO can be caused by the combined effect of crystal distortion and oxygen vacancies. Local imperfections can thus be a major contribution to the dielectric anomaly in STO induced by bending.

**Local ferroelectric order induced in STO thin films**

We studied STO thin films grown on different substrates using both X-ray diffraction and Ti *K*-edge X-ray absorption spectroscopy. By analyzing the data from XRD and EXAFS, we found that sputtered STO thin films retain their crystallinity, like standard STO powders, which is totally different from amorphous and preferentially oriented films. The Ti *K*-edge spectra reveal a large enhancement of the $e_g$ peak, indicating the emergence of local polarization and lower symmetry. We also observed two minor changes in the spectra depending on the films: (1) an enhancement of the main absorption edge and (2) a clear separation between the $e_g$ and $t_{2g}$ peaks. Moreover, we observed these two effects for different films due to the effects of lattice mismatch. In comparing the XANES and the partial DOS of Ti 3*d* and O2*p*, including both Ti displacement and $TiO_6$ octahedral rotation, our finite-difference simulations were in good agreement with experiment, and we showed that local FE order caused by the Ti off-centering and AFD order due to the $TiO_6$ octahedra coexist in STO thin films. Our

results may inspire sputtered-STO applications in lead-free ferroelectric memory devices.

To sum up the above conclusions, for the pure quantum paraelectric STO, the local ferroelectric order with the microscopic view was clarified from XAFS and RXES spectra. The STO single crystals both under uniaxial and bending pressure are shown to be substantially free of FE transformation in local region. On the contrary, the sputtered STO thin film is confirmed the character of local FE transition as the Ti off-center displacement is investigated as well as the AFD distortion. Consistent with the above findings, it is qualitatively clear that exploration of the intrinsic FE transition in STO single crystal using the external pressure is not easy to implement but in other structural patterns of STO such as thin films is feasible to achieve. We expect much more appropriated study can be access on STO to get ferroelectric properties in the near future.

# Acknowledgment

First, I would like to give special appreciation to my supervisor Prof. Hiroshi Maruyama who allowed the opportunities for me to study in such a favorable environment and participate in pioneering research on the structure and dielectric characterization of perovskite oxides materials. I would like to express my grateful gratitude to Prof. Nobuo Nakajima especially. During my doctoral period, his patient and intellectual guidance enlightened me a lot and motivated me to promote my scientific research. The helpful advice, support, and friendship from Prof. Nobuo Nakajima is not only precious to my academic level but to my daily life and personality as well. I also would like to appreciate Dr. Naoki Ishimatsu who offered me valuable comments and suggestions with my research as well as concern on my life. Their profound knowledge, rigorous academic attitude, keen scientific insight, and the spirit of exploration of science will be the model for me in my whole life.

I would like to acknowledge the great support for XAFS and RXES experiments from the beamline scientists from SPring-8, Dr. Naomi. Kawamura and Dr. Motohiro. Suzuki. Moreover, the staff of Photon Factory are acknowledged for their excellent instrumental operation.

I shall thank Prof. Yoshihiro Kuroiwa who gave me an opportunity to make the oral presentation on the Japan-Korea workshop and provided many beneficial comments on my research work. I thank all the staff of physical science office and student support office of graduate school of science for helping me with paper works, information sharing, and scholarship recommendation.

I would like to thank all members of our laboratory; Mr. S. Kawakami, Mr. Y. Yamane Mr. Y. Sata, Ms. K. Fujii, Mr. A. Sano, Mr. C. Temba, Mr. K. Moriai, Mr. T. Naito, Mr. T. Kumamoto, Mr. T. Kawauchi, Mr. Y. Nakamura, Mr. K. Mine, Mr. S. Ono, Mr. Y. Yamanaka, Mr. K. Yokoyama, Mr. K. Ohshiro, Mr. Y. Noji, Mr. D. Miyashita, Mr.

T. Toriyu, Mr. K. Ehara, Mr. S. Kato, Ms. M. Kousa, and Mr. S. Iwasaki. As an oversea student, with your help and friendship, I quickly adapted to the environment of learning and living in Japan and kept on well my research work. I enjoyed getting along with you and I will never forget the happy time we worked and play together. I also send my gratitude to Japan student services organization, YAHATA and KUMAHIRA, for providing scholarships for the financial support.

Thanks very much to my best friends, Jiaying Hu and Yunfeng Ma, who encouraged me when I was confused and depressed. They were willing to listen to my thoughts and gave me enormous support in my doctoral study period.

Finally, I owe my parents a lot of thanks specially. Without their spiritual and economic supplements from China, I will not have the achievements in research today.

I must say that I feel most honored and happy to be a member of our laboratory and a student of my three teachers. どうもありがとうございます！

# Reference


[1] Vasala S. and Karppinen M. 2015 *Prog. Solid State Ch.* **43** 1.

[2] Stern E. A. 2004 *Phys. Rev. Lett.* **93** 037601.

[3] Zhou K J. Radovic M. Schlappa J. Strocov V. Frison R. Mesot J. Patthey L. and Schmitt T. 2011 *Phys. Rev. B* **83** 201402.

[4] Kimura T., Goto T., Shintani H., Ishizaka K., Arima T. and Tokura Y. 2003 *Nature* **426** 55.

[5] Rabe K., Ahn C. H., and Triscone J. M. *Physics of Ferroelectrics: A Modern Perspective* (Springer, Berlin, 2007).

[6] Evarestov R. A., Blokhin E., Gryaznov D., Kotomin E. A. and Maier J. 2011 *Phys. Rev. B* **83** 134108.

[7] Chang Y. J., Khalsa G., Moreschini L. Walter A. L., Bostwick A., Horn K., MacDonald A. H. and Rotenberg E. 2013 *Phys. Rev. B* **87** 115212.

[8] Mannhart J. and Schlom D. G. 2010 *Science* **327** 1607.

[9] Leisegang T., Stoecker H., Levin A. A., Weissach T., Zschornak M., Gutmann E., Rickers K., Gemming S. and Meyer D. C. 2009 *Phys. Rev. Lett.* **102** 088103.

[10] Chang Y. J., Bostwick A., Kim Y. S., Horn K. and Rotenberg E. 2010 *Phys. Rev. B* **81** 4.

[11] Ohta H., Kim S., Mune Y., Mizoguchi T., Nomura K., Ohta S., Nomura T., Nakanishi Y., Ikuhara Y., Hirano M., Hosono H. and Koumoto K. 2007 *Nat Mater* **6** 129.

[12] Unoki H. and Sakudo T. 1967 *J. Phys. Soc. Jpn.* **23** 546.

[13] Muller K. A., Berlinger W. and Tosatti E. 1991 *Z. Phys. B* **84** 277.

[14] Kan D. S., Terashima T., Kanda R., Masuno A., Tanaka K., Chu S. C., Kan H., Ishizumi A., Kanemitsu Y., Shimakawa Y. and Takano M. 2005 *Nat. Mater.* **4** 816.

[15] Kan D., Kanda R., Kanemitsu Y., Shimakawa Y., Takano M., Terashima T. and

Ishizumi A. 2006 *Appl. Phys. Lett.* **88** 191916.

[16] Nozawa S., Iwazumi T. and Osawa H. 2005 *Phys. Rev. B* **72** 4.

[17] Yamamoto T. 2008 *X-Ray Spectrom.* **37** 572.

[18] Nozawa S., Iwazumi T., Osawa H. and Uozumi T. 2013 *Appl. Phys. Express* **6** 4.

[19] Nakajima N., Oki M., Isohama Y., Maruyama H., Tezuka Y., Ishiji K., Iwazumi T. and Okada K. 2012 *Phys. Rev. B* **86** 224114.

[20] Haeni J. H., Irvin P., Chang W., Uecker R., Reiche P., Li Y. L., Choudhury S., Tian W., Hawley M. E., Craigo B., Tagantsev A. K., Pan X. Q., Streiffer S. K., Chen L. Q., Kirchoefer S. W., Levy J. and Schlom D. G. 2004 *Nature* **430** 758.

[21] Nakano T., Mikami Y., Abe K., Suzuki S., Akiyama K. and Ando A. 2014 *Ferroelectrics* **464** 72.

[22] Itoh M., Wang R., Inaguma Y., Yamaguchi T., Shan Y. J. and Nakamura T. 1999 *Phys. Rev. Lett.* **82** 3540.

[23] Taniguchi H., Yagi T., Takesada M. and Itoh M. 2005 *Phys. Rev. B* **72**.

[24] Jang H. W., Kumar A., Denev S., Biegalski M. D., Maksymovych P., Bark C. W., Nelson C. T., Folkman C. M., Baek S. H., Balke N., Brooks C. M., Tenne D. A., Schlom D. G., Chen L. Q., Pan X. Q., Kalinin S. V., Gopalan V., and C. B. Eom C. B. 2010 *Phys. Rev. Lett* **104** 197601.

[25] Dove M. T. *Structure and Dynamics: An Atomic View of Materials* (OUP Oxford, Oxford, 2003).

[26] Kawakami S., Nakajima N., Takigawa T., Nakatake M., Maruyama H., Tezuka Y. and Iwazumi T. 2013 *J. Phys. Soc. Jpn.* **82** 053701.

[27] Kawakami S., Nakajima N., Nakatake M., Kawamura N., Mizumaki M. and Maruyama H. 2015 *Jap. J. Appl. Phys.* **54** 10NC03.

[28] Temba C., Kawakami S., Nakajima N., Ishimatsu N. and Maruyama H. 2015 *J. Kor. Phys. Soc.* **66** 1386.

[29] Scott J. F. 2013 *J. Phys.: Condens. Matter* **25** 415901.

[30] Nguyen T. D., Mao S., Yeh Y. W., Purohit P. K. and McAlpine M. C. 2013 *Adv*

*Mater* **25** 946.

[31] Cross L. E. 2006 *J. Mater. Sci.* **41** 53.

[32] Tagantsev A. K. 1987 *Uspekhi Fizicheskikh Nauk* **152** 423.

[33] Xu T., Wang J., Shimada T. and Kitamura T. 2013 *J. Phys.: Condens. Matter* **25** 415901.

[34] Zubko P., Catalan G., Buckley A., Welche P. R. and Scott J. F. 2007 *Phys. Rev. Lett.* **99** 167601.

[35] Fujii Y., Uwe H. and Sakudo T. 1987 *J. Phys. Soc. Jpn.* **56** 1940.

[36] Schneider T., Beck H. and Stoll E. 1976 *Phys. Rev. B* **13** 1123.

[37] Tsujimi Y., Minami H. and Uwe H. 2012 *Ferroelectrics* **430** 50.

[38] Frenkel A. I., Ehre D., Lyahovitskaya V., Kanner L., Wachtel E. and Lubomirsky I. 2007 *Phys Rev Lett* **99** 215502.

[39] Wachtel E. and Lubomirsky I. 2010 *Adv. Mater.* **22** 2485.

[40] Woicik J. C., Shirley E. L., Hellberg C. S., Andersen K. E., Sambasivan S., Fischer D. A., Chapman B. D., Stern E. A., Ryan P., Ederer D. L. and Li H. 2007 *Phys. Rev. B* **75**.

[41] Calvin S. *XAFS for Everyone* (CRC Press, Boca Raton, 2013).

[42] Bunker G. *Introduction to XAFS* (Cambridge Universuty Press, Cambridge, 2010).

[43] Yano J. and Yachandra V. K. 2009 *Photosynth. Res*. **102** 241.

[44] Ament L. J. P., van Veenendaal M., Devereaux T. P., Hill J. P. and van den Brink J. 2011 *Rev. Mod. Phys.* **83** 63.

[45] Ishii K., Tohyama T. and Mizuki J. 2013 *J. Phys. Soc. Jpn.* **82** 24.

[46] Isohama Y., Nakajima N., Watanabe G., Mizumaki M., Kawamura N. and Maruyama H. 2011 *Jap. J. Appl. Phys.* **50** 09NE04.

[47] Agui A., Uozumi T., Mizumaki M. and Kaambre T. 2009 *Phys. Rev. B* **79** 4.

[48] Willmott P. *An Introduction to Synchrotron Radiation* (Wiley, West Sussex, 2011).

[49] Mobilio S., Boscherini F. and Meneghini C. *Synchrotron Radiation: Basics, Methods and Applications* (Springer, Berlin, 2015).

[50] SPring-8. http://www.lightsources.org/facility/spring8

[51] Toyokawa H., Broennimann C., Eikenberry E. F., Henrich B., Kawase M., Kobas M., Kraft P., Sato M., Schmitt B., Suzuki M., Tanida H. and Uruga T. 2010 *Nucl. Instrum. Meth. A* **623** 204.

[52] SPring-8. BL39XU. http://www.spring8.or.jp/wkg/BL39XU/instrument/lang-en/INS-0000000312/instrument_summary_view

[53] Photon Factory. http://www.lightsources.org/facility/pf

[54] Photon Factory. BL-9A. http://pfwww.kek.jp/inada/xafsbl/9a/bl9a_e.html

[55] Uozumi T., Okada K., Kotani A., Durmeyer O., Kappler J. P., Beaurepaire E. and Parlebas J. C. 1992 *Europhys. Lett.* **18** 85.

[56] Itie J. P., Couzinet B., Dhaussy A. C., Flank A. M., Jaouen N., Lagarde P. and Polian A. 2006 *High Pressure Res.* **26** 325.

[57] Vedrinskii R. V., Kraizman V. L., Novakovich A. A., Demekhin P. V. and Urazhdin S. V. 1998 *J. Phys.: Condens. Matter* **10** 9561.

[58] Itie J. P., Couzinet B., Polian A., Flank A. M. and Lagarde P. 2006 *Europhys. Lett.* **74** 706.

[59] Ankudinov A. L., Ravel B., Rehr J. J. and Conradson S. D. 1998 *Phys. Rev. B* **58** 7565.

[60] Buban J. P., Iddir H. and Ogut S. 2004 *Phys. Rev. B* **69** 4.

[61] Stöcker H., Hanzig J., Zschornak M., Mehner E., Jachalke S., Richter C., Hanzig F., Meutzner F., Leisegang T. and Meyer D. C. 2017 *Cryst. Res. Technol.* **52** 1600222.

[62] Aschauer U. and Spaldin N. A. 2014 *J. Phys.: Condens. Matter* **26** 122203.

[63] Yamada T., Eerd B. W., Sakata O., Tagantsev A. K., Morioka H., Ehara Y., Yasui S., Funakubo H., Nagasaki T. and Trodahl H. J. 2015 *Phys. Rev. B* **91** 214101.

[64] Bunau O. and Joly Y. 2009 *J. Phys.: Condens. Matter* **21** 345501.

[65] Stoecker H., Zschornak M., Richter C., Hanzig J., Hanzig F., Hinze A., Potzger K., Gemming S. and Meyer D. C. 2014 *Scripta Mater.* **86** 1.

[66] Lee D., Yoon A., Jang S. Y., Yoon J. G., Chung J. S., Kim M., Scott J. F. and Noh T. W. 2011 *Phys. Rev. Lett.* **107**.

[67] Tyson T. A., Yu T., Croft M., Scofield M. E., Bobb-Semple Dara, Tao Jing, Jaye Cherno, Fischer Daniel and Wong Stanislaus S. 2014 *Appl. Phys. Lett.* **105** 091901.

# 公表論文

**(1) Observation of the flexoelectricity of a $SrTiO_3$ single crystal by X-ray absorption and emission spectroscopies**

**Cong Lu**, Nobuo Nakajima, and Hiroshi Maruyama

Journal of Physics: Condensed Matter 29 (2017) 045702.

**(2) Isotropic Shrinkage of the Oxygen Octahedron in $SrTiO_3$ under Uniaxial Pressure**

**Cong Lu**, Chisato Temba, Nobuo Nakajima,
Shuhei Kawakami, Naoki Ishimatsu, and Hiroshi Maruyama

Journal of Physics: Condensed Matter, Accepted on 10 July 2017.

# 参考論文


**(1) Dielectric characteristics of cation deficient $TbMnO_3$**

**Cong Lu**, Yimin Cui

Physica B: Condensed Matter **407** (2012) 3856.

**(2) Dielectric characteristics of Si-added and Si-doped $TbMnO_3$**

**Cong Lu**, Yimin Cui

Physica B: Condensed Matter **432** (2014) 58.